TRANSPORT AND MAGNETIC PROPERTIES OF RTX AND RELATED COMPOUNDS

A Dissertation

by

VENKATESHWARLU GORUGANTI

Submitted to the Office of Graduate Studies of
Texas A&M University
in partial fulfillment of the requirements for the degree of

DOCTOR OF PHILOSOPHY

December 2008

Major Subject: Physics

TRANSPORT AND MAGNETIC PROPERTIES OF RTX AND RELATED

COMPOUNDS

A Dissertation

by

VENKATESHWARLU GORUGANTI

Submitted to the Office of Graduate Studies of
Texas A&M University
in partial fulfillment of the requirements for the degree of

DOCTOR OF PHILOSOPHY

Approved by:

Chair of Committee,   Joseph H. Ross, Jr
Committee Members,   Glenn Agnolet
                                   Donald G. Naugle
                                   Raymond E. Schaak
Head of Department,   Edward Fry

December 2008

Major Subject: Physics

ABSTRACT

Transport and Magnetic Properties of RTX and Related

Compounds. (December 2008)

Venkateshwarlu Goruganti, B.Sc., B.Ed., Osmania University, India;

M.Sc., University of Hyderabad, India;

M.S., Texas A&M University

Chair of Advisory Committee: Dr. Joseph H. Ross, Jr.

Physical properties of RTX compounds (R = Rare earth, T = Transition metal and X = main group element from B, C or N group) compounds have been studied by means of electrical resistivity, heat capacity, dc magnetization and NMR. Searching for new magnetic materials is always an interesting topic from both a technological and basic research prospective; it is even more interesting when unusual magnetic phases are observed. Ternary intermetallic plumbides are interesting because of their unconventional magnetic ordering and variety of multiple magnetic transitions. Crystalline electric fields (CEF) also strongly effect the magnetic properties of these intermetallics. To understand the phase transitions, CEF effects, and magnetic interactions, a systematic study of the RNiPb, R_2Ni$_2$Pb, R_5NiPb$_3$ and RCuGe systems were conducted.

Among the results for NdNiPb a single antiferromagnetic transition was found at 3.5K, while the superconductivity found in some ingots of this material was shown not to correspond to a bulk behavior for this phase. Nd$_2$Ni$_2$Pb was shown to have a canted zero field magnetic structure with a low temperature metamagnetic transition 3 T. In NdCuGe, a 3K AF transition was found along with a corresponding magnon contribution to the specific heat and magnetic and thermodynamic behavior from

which the detailed CEF configuration was obtained.

In a series of measurements on recently-synthesized $R_5\text{NiPb}_3$ (R=Ce, Nd, Gd), for Ce_5NiPb_3 a transition at 48 K was found, which was confirmed to be ferromagnetic character from field dependent heat capacity and Curie-Weiss susceptibility. Nd_5NiPb_3 exhibits two transitions, an antiferromagnetic transition at 42 K and an apparently weak ferromagnetic canting transition at 8 K. For Gd_5NiPb_3, a ferro- or ferrimagnetic transition was found at 68 K. For the Ce and Nd materials metamagnetism was also observed at low temperatures. In addition, very large metallic type γ terms were found in the specific heat, as well as a reduced value of the magnetic entropy, for all three systems. These results imply a lack of ordering for one of the two in-equivalent chains in these materials. This is discussed in terms of possible geometrical frustration on one of the spin chains.

To My Parents

ACKNOWLEDGMENTS

I would like express my gratitude and sincere thanks to my advisor Dr. Joseph H. Ross, Jr., for his tremendous support and encouragement. I enjoyed all the fruitful discussions with him throughout my Ph.D. period. I would not have accomplished this without his feedback.

I thank my committee members for their input.

I thank Dr. Donald G. Naugle and Dr. Dayar Rathanyaka for letting me use their PPMS and Arc melting facility. I thank the Chemistry Department for maintaining the SQUID and x-ray facility. I thank Dr. Ray Guillemette for helping me with micro probe measurements. I thank our colloborator Dr. Oner from Turkey for valuable discussions and for providing some samples.

I thank our group members, Dr. Yang Li, Dr. Weiping Gou, Dr. Ji Chi, Sergio Y. Rodriguez and others, for their support.

My parents, Satyanarayana Rao and Pramila, have always encouraged me to excel in higher education. Their support and encouragement have meant a lot to me and they are a huge part of whatever I am and become in life. I also thank my sister Rajita and my grandmother for their inspiration and support.

Special thanks to my wife Rama and my son Sujan for their support, patience and understanding.

I would like to thank Dr. Anil K. Bhatnagar for encouraging me to enroll at Texas A&M University.

Last but not least I would like to acknowledge the Robert A. Welch foundation and the Physics Department for the financial support during my Ph.D. studies.

TABLE OF CONTENTS

LIST OF FIGURES

FIGURE   Page

CHAPTER I

INTRODUCTION

A. Overview

Intermetallic compounds containing rare earth elements are interesting because they exhibit a variety of magnetic ordering behavior depending on the ratio of exchange interactions to crystal field interactions. Apart from a variety of magnetic properties, these materials also can show mixed valence, heavy Fermion, spin glass [1, 2] and superconducting behavior coexisting with long range magnetic ordering. Hence rare earth intermetallic compounds have been the subject of many recent experimental investigations because of the nature and variety of their physical and magnetic properties. In particular ternary intermetallic plumbides are interesting because of their unconventional magnetic ordering and variety of multiple magnetic transitions [3].

The purpose of this section is to summarize information to date, derived from recent experimental investigations, of the magnetic behavior of ternary intermetallic compounds. Much of this work will be concentrated on Cu and Ni based plumbides and germanides with the general formula RTPb and RTGe, where R = rare earth element and T = Ni and Cu. Not many measurements have been done on these compounds, although ternary equiatomic lanthanide silicides and germanides with the general formula RTSi and RTGe crystallized in several crystal structure types have been studied extensively [4].

———————

This dissertation follows the style of *Journal of Applied Physics.*

In such materials, the competition between exchange interactions and crystal field splitting can give rise to complex magnetic structures and to unusual magnetization processes [2, 5]. The exchange interaction between the localized moments can be mediated through the conduction electrons. This typically occurs when a localized spin polarizes the conduction electrons, which couple to a neighboring moment at a distance r. This is known as the RKKY (Ruderman, Kittel, Kasuaya and Yosida) interaction. It is a long range interaction and has an oscillatory spacial dependence [6]. Depending on the separation, the sign of the magnetic coupling may be either ferromagnetic or antiferromagnetic. The RKKY type interaction is generally the dominant mechanism for rare-earth magnetic ordering.

B.   Materials of Interest

Very recently, a new series of ternary intermetallic compounds RNiPb (111) [7] and R_2Ni_2Pb (221) [8, 9] was synthesized by Gulay *etal*. The 221 crystal structure is highly anisotropic and possesses layered structure. Giant magnetoresistance was observed in the Er, Ho and Dy members of this series [10], and anisotropic magnetic properties in the $R =$ Gd and Tb members [11]. The 111 type plumbides crystallize in the TiNiSi-type structure.

1. RNiPb

The initial motivation behind studying this material was the possible coexistence of superconductivity and antiferromagnetism. In preliminary studies of NdNiPb in our laboratory, superconductivity was observed at a temperature below a magnetic transition. My studies demonstrate that this is not due to NdNiPb, and may be due to an alternative phase, as described in a later chapter. RNiPb type plumbides
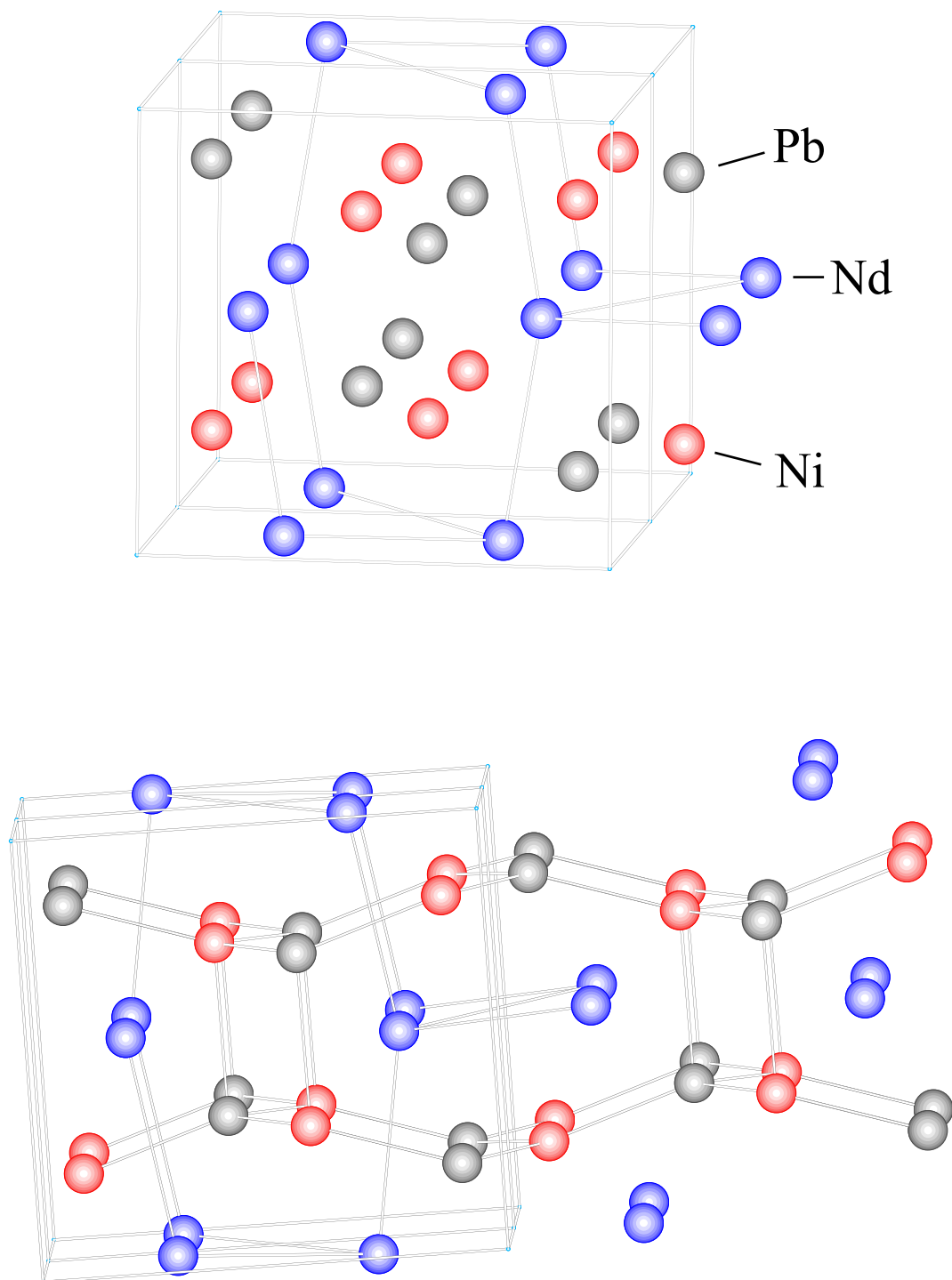
Fig. 1. NdNiPb structure, showing the naturally occurring channels.

which crystallize in the TiNiSi-type structure, here $Pnma$ space group (# 62). This structure has a naturally occurring channel configuration, which is shown in Fig. 1

2. R_2Ni_2Pb

R_2Ni_2Pb was synthesized by Gulay *et al.* [8] with R = Y, Sm, Gd, Tb, Dy, Ho, Er, Tm and Lu. These compounds crystallize in the AlB_2Mn_2-type structure, with the $Cmmm$ space group (# 65), and are interesting because of their unconventional magnetic ordering and multiple magnetic transitions. The crystal symmetry is highly anisotropic and possesses a layered structure [8]. Giant magnetoresistance was observed in the Er, Ho and Dy members of this series [10], and anisotropic magnetic properties in the R = Gd and Tb members [11]. Nd_2Ni_2Pb was also shown separately to form in the R_2Ni_2Pb structure [9]. Fig. 2 shows the Nd_2Ni_2Pb unit cell showing the naturally occurring multilayer with planes of Nd and Pb atoms and a wavy plane of Ni atoms. All Nd atoms in the unit cell are crystallographically equivalent. In this disertation I focus upon the low temperature magnetic properties of Nd_2Ni_2Pb through magnetization and heat capacity measurements [12].

3. RCuGe

Ternary equiatomic lanthanide silicides and germanides with the general formula RTSi and RTGe (R = rare earth; T = transition metal) crystallize in several different structure types and have been studied extensively [4, 13, 14]. RCuGe type samples were found to have the AlB_2 structure (space group designation $P6/mmm, \#191$) as reported by Iandelli [15]. In Fig. 3 the RCuGe crystal structure is shown [16]. In spite of numerous experimental studies of these compounds, there are limited reports about the behavior of the RCuGe system.

Recent work from our group included magnetization, resistivity and thermal
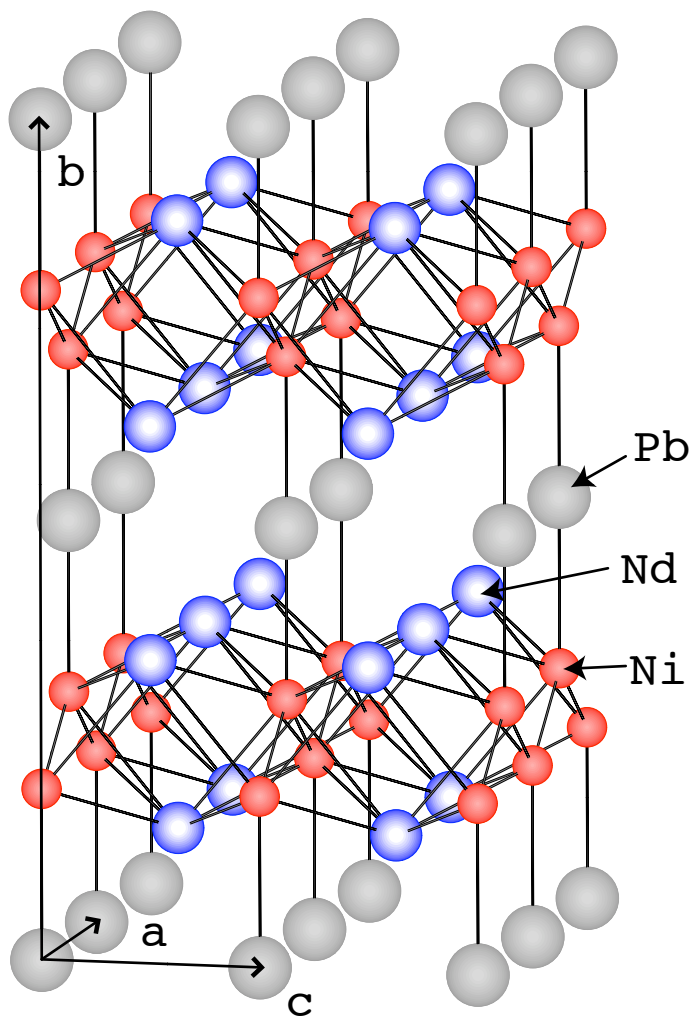
Fig. 2. Nd$_2$Ni$_2$Pb structure. Four cells are shown, viewed along the a axis, showing the naturally occurring layered structure.
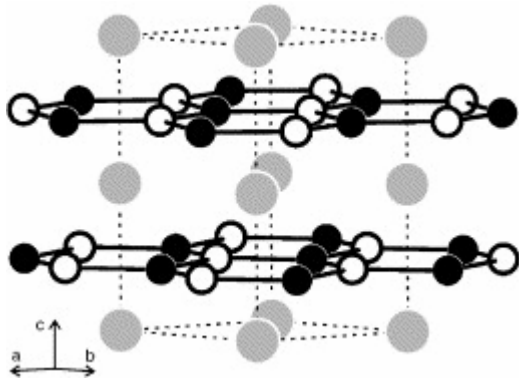
Fig. 3. RCuGe layered structure, in which R atoms (grey) are separated by Cu-Ge network

transport measurements on CeCuGe, that crystallize in the hexagonal AlB$_2$-type structure [17]. This compound was found to be magnetically quite soft, with a very small magneto-crystalline anisotropy, contrary to what was reported in a previous investigation [18]. In this work, I present magnetic, thermal and transport properties of NdCuGe [19], shown to have an antiferromagnetic transition at 3.4 K by neutron scattering measurements [20], and will compare these to CeCuGe. Although the crystallographic structures of these compounds are identical, I found their electronic and thermal transport properties to be quite different in some respects. For example, while CeCuGe exhibits a ferromagnetic transition at $T_c = 10$ K strongly influenced by spin fluctuations [17], NdCuGe has its antiferromagnetic transition at 3.4 K, associated with the alignment of crystal-field-split levels of the magnetic Nd ion, and transport properties much closer to those of a classic metallic system.

4. R_5NiPb$_3$

Ternary Ni based plumbides with the general formula R_5NiPb$_3$ [21] ($R =$ rare earth) have been discovered very recently. Except for the recent report on Nd$_5$NiPb$_3$ [22]

by our group, the $R_5\text{NiPb}_3$ system has not been studied. In Fig. 4 the $R_5\text{NiPb}_3$ crystal structure is shown. It adopts the hexagonal Hf_5CuSn_3-type structure. In this structure the R atom has two sites, $4d$ and $6g$, one of which forms triangular anti-pyramid chains. When viewed along the c-axis, in the diamond shaped unit cell, half of which makes an equilateral triangle, the center of the triangle is occupied by one of the R sites ($4d$), while Ni atoms sit at the corners of the triangle surrounded by R atoms of the antipyramidal chains. It is clearly shown in the bottom of Fig. 4.

C.   Present Problems of Rare-Earth Intermetallics

Searching for new magnetic materials is always an interesting topic from a technological and basic research prospective; it is even more interesting when unusual magnetic phase transitions are observed. In particular ternary intermetallic plumbides are interesting because of their unconventional magnetic ordering and variety of multiple magnetic transitions. At the same time understanding the fundamental cause of these materials properties is also important.

In ternary rare-earth compounds the R ion sits distributed through the lattice and has a partially filled $4f$ shell with a corresponding magnetic moment. Since these compounds are usually metallic in nature, R moments are coupled via the RKKY interaction. This can lead to a long range ordering of moments and well defined features in the physical properties. In some materials, these interactions can lead to a Kondo effect where these localized spins form a pseudo-singlet state with the conduction electron cloud. This can lead to well defined features in physical properties; there can be a minimum and upturn in the electrical resistivity curve at low temperature and a reduction in the effective magnetic moment.

The $4f$ electrons of R ions are deep inside the core, and being surrounded by
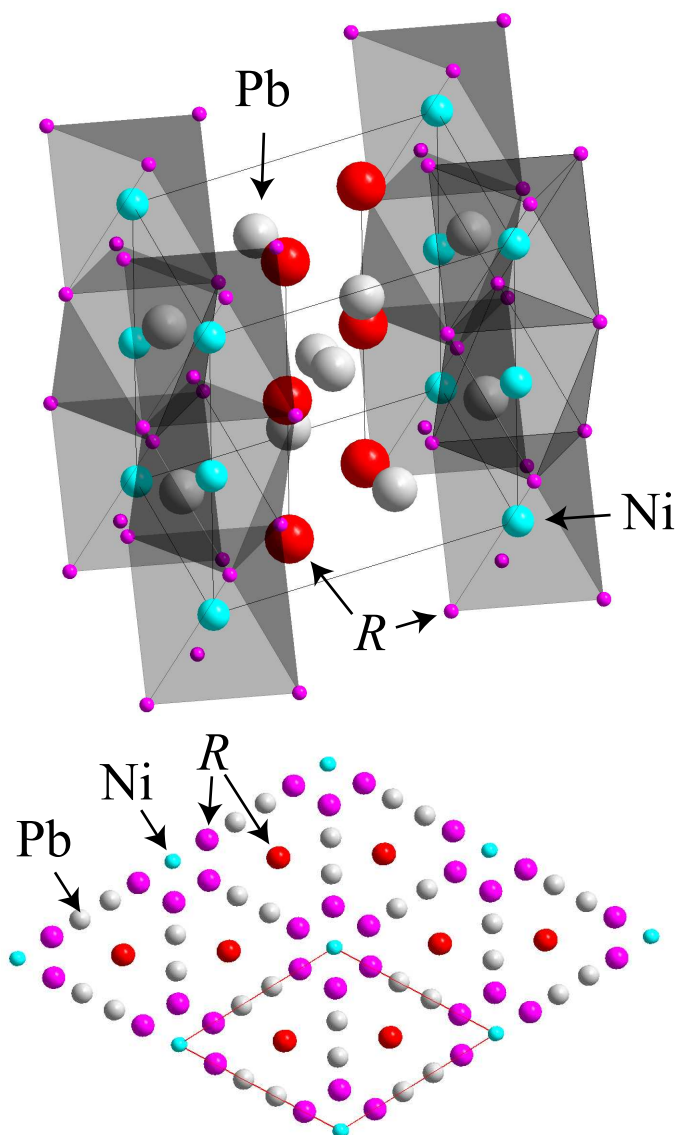
Fig. 4. Top: R_5NiPb_3 structure; one hexagonal unit cell shown with extra R atoms added to indicate the chain configuration. Bottom: View of structure anlong c-axis, with small spheres = Ni, dark grey large spheres = R.

the $5s$ and $5p$ orbitals, do not participate significantly in chemical bonding. For most cases the $4f$ electrons are responsible for the magnetic properties of rare-earth materials. The spin orbit coupling is strong enough in rare-earths hence the total angular momentum J is a good quantum number rather than L and S. This parameter is determined by Hund's rules, which will be discussed later. The unperturbed ground state of the rare-earth ion will be $2J + 1$-fold degenerate; however, when the ion is placed in a lattice, it will see inhomogeneous electric fields produced by its neighbors, which introduce level splittings. These fields are known as crystalline electric fields (CEFs). CEFs at the rare earth site thus can strongly affect the magnetic properties. In $3d$ shell electrons the CEF has an even larger magnitude due to the large radius of $3d$ orbitals and the absence of any outer electronic shells to screen the $3d$ shell. On the other hand the CEF's strength is particularly small whenever there is approximate spherical symmetry, for example Gd^{3+} has $L = 0$ ($^8S_{7/2}$), hence the symmetric occupation of electron orbitals in Gd compounds means that the CEF is minimal. More details of CEF will be given in chapter III.

To understand the phase transitions, CEF effects, complex magnetic interactions and ground states of these materials, I carried out a systematic study of several rare earth intermetallics using multiple experimental means. In this study I report the results on $R\mathrm{NiPb}$, $R\mathrm{CuGe}$ and $R_5\mathrm{NiPb}_3$. We performed magnetization, heat capacity and resistivity measurements on these materials at temperatures between 2 and 350 K and in magnetic fields up to 8 T. Through the heat capacity measurements I identified a number of phase transitions. For some materials we subtracted electron and phonon heat capacities using the non-magnetic analogs, La or Y based samples, to obtain the magnetic contributions to the heat capacity. In several cases this allowed observation of a broad Schottky anomaly in addition the phase transition, providing a measure of the CEF effects. In some cases the entropy was used to provide further information

about the ground state. Magnetization data is also sensitive to CEF splitting, and I used the CEF values obtained from the heat capacity data to fit magnetization data to further define the magnetic behavior.

Among the results obtained from this research, for NdNiPb a single antiferromagnetic transition was observed at 3.5 K. Although superconductivity had been reported in some samples of this material, I found this not to be a bulk behavior for this phase. Nd_2Ni_2Pb has a canted zero field magnetic structure, with a metamagnetic transition to an aligned phase occurring in $H = 3$ T at low temperatures. In NdCuGe, we obtained a spontaneous moment somewhat larger than reported from neutron scattering, the difference attributed to intrinsic site-occupation disorder. In the R_5NiPb_3 materials, I observed a variety of magnetic transitions; however, the associated magnetic entropy is consistently smaller than expected. I also observed an unusually large linear contribution to the specific heat. Based on the geometry of R_5NiPb_3 structure I proposed a frustrated magnetic model which may account for these results.

CHAPTER II

HEAT CAPACITY

Observations of the heat capacity can be important for determining the magnetic properties of solids. In this chapter, I discuss the basic theory of and different contributions to the total heat capacity. Dulong and Petit predicted that the specific heat for most solids at room temperature is 24.9 mJ/(mole-K). This can be explained by the equipartition theorem; each atom can be viewed as an independent oscillator with average kinetic energy $\frac{3}{2}k_B T$ and average potential energy $\frac{3}{2}k_B T$. The average total energy per mole is thus $3Nk_B T$ where N is Avogadro's number. Therefore the heat capacity is $C_v = 3Nk_B = 3R$ where $R = Nk_B$ is the ideal gas constant. Often I use this as a check to see whether my sample structure and number of atoms per formula unit is consistent with the measured and classical limit of heat capacity. In summary the classical heat capacity follows

$$C_v = \frac{\partial U}{\partial T} = 3Nk_B T = 3R. \tag{2.1}$$

But the heat capacity at low temperature varies and goes to zero as the temperature goes to zero. This cannot be explained by the classical concept of degrees of freedom; however, more detailed quantum mechanical mechanisms described below provide an explanation.

A.   Lattice Heat Capacity

Quantized lattice vibrations are called phonons. Debye was successful in explaining the low temperature phonon heat capacity [23]. The fundamental assumption in the Debye model is that the solid can be treated as an isotropic elastic continuum for all possible vibrational modes. This assumption worked very well at low T because the

wavelengths of low energy modes are much greater than the inter-atomic distance for low k and therefore crystals approach a continuum. At low k all solids have acoustic phonons which have a dispersion relation

$$\omega = ck$$

leading to the corresponding density of phonon modes,

$$D(\omega) = \frac{V\omega^2}{2\pi^2 c^3}. \tag{2.2}$$

This leads to the Debye phonon heat capacity,

$$C_v = 9nR \left(\frac{T}{\Theta_D}\right)^3 \int_0^{x_D} \frac{x^4 e^x dx}{(e^x - 1)^2} \equiv 9nR \left(\frac{T}{\Theta_D}\right)^3 D\left(\frac{\Theta_D}{T}\right), \tag{2.3}$$

where n is the number of atoms per formula unit, $x_D = \Theta_D/T$, and Θ_D is the Debye temperature which corresponds to a cutoff frequency. According to the Debye model, modes above the frequency $(k_B \Theta_D/\hbar)$ are not permitted. $D\left(\frac{\Theta_D}{T}\right)$ is known as the Debye integral.

For the case where $T << \Theta_D$

$$C_v = \frac{12\pi^4}{5} \left(\frac{nR}{\Theta_D^3}\right) T^3 \equiv \beta T^3 \tag{2.4}$$

where $\beta = \left(\frac{1943.7n}{\Theta_D^3}\right)$ J/mol.K^4 with Θ_D in K. By extracting β from heat capacity data we can get the Debye temperature Θ_D. Equation 2.4 is the well-known Debye T^3-law. It works very well at low T but departs at high T because of the deviation of $D(\omega)$ from the assumed ω^2-dependence, as the heat capacity crosses over to the Dulong-Petit limit.

B. Electronic Heat Capacity

Even though the electronic contribution to the total heat capacity is small ($< 1\%$) at room temperature, it is very significant at low temperature since other terms die out very quickly. In a metal, only those electrons close to the Fermi level, within the approximate range $k_B T$ of the Fermi energy, contribute to the specific heat. The effective number of electrons in this energy range is proportional to T and each electron in this region contributes roughly an amount $\frac{3}{2}k$ to the heat capacity. Hence the electronic heat capacity is linearly proportional to T. Consequently

$$C_v = \gamma T, \tag{2.5}$$

where the proportionality constant γ is [24]

$$\gamma = \frac{m}{\hbar}(N)^{1/3}(\frac{\pi V_m}{3})^{2/3}k_B^2. \tag{2.6}$$

For a typical metal, Cu, $V_m \approx 7$ cm^3/mol which corresponds to γ=0.5 mJ/mole.K^2. The measured value, γ=0.69 mJ/mole.K^2 [6] approximately agrees with this simple theory. Therefore at low-T the total heat capacity can be expressed in the following limiting form:

$$C_v = \gamma T + \beta T^3. \tag{2.7}$$

Therefore in some cases I used the standard method of analyzing the specific heat experimental data at low-T by plotting C_v/T vs. T^2 and by fitting to a straight line according to $C_v/T = \gamma + \beta T^2$. Extracting the value for the slope β yields Θ_D, and the intercept γ yields information about the electron density of states.

C. Magnetic Heat Capacity

In addition to lattice and electronic heat capacity, additional contributions can also arise from various magnetic excitations. These will have distinctive characteristic temperature dependences. Thermal excitation of spin waves gives one such magnetic heat capacity contribution. Quantized spin waves are called magnons, and there are two main types of magnons depending on magnetic order; ferromagnetic (FM) and antiferromagnetic (AF) magnons. Also the intermediate case, ferrimagnetic, typically behaves similar to AF. The two types of magnons have different dispersion relations and hence different temperature dependences for heat capacity.

1. FM Magnons

FM magnons have the following dispersion relation for small q (spin wave vector)

$$\omega_q \propto q^2, \tag{2.8}$$

yielding a corresponding low frequency density of magnon modes,

$$\eta(\omega) \propto \sqrt{\omega}. \tag{2.9}$$

Hence the FM heat capacity will have the contribution,

$$C_M = S_f R \left(\frac{k_B T}{2JS} \right)^{3/2}. \tag{2.10}$$

In this relationship, J is the exchange term, S is is the spin angular momentum and the constant S_f, which depends on crystal structure, has been calculated for several types of lattice [23, 25]

2. AFM Magnons

AFM magnons have the following low-q dispersion relation

$$\omega_q \propto q, \tag{2.11}$$

yielding a corresponding density of magnon modes,

$$\eta(\omega) \propto \omega^2. \tag{2.12}$$

In this case the AFM material's low-T magnetic heat capacity corresponds to,

$$C_M = S_{af} R \left(\frac{k_B T}{2 J' S} \right)^3. \tag{2.13}$$

In this case, similar to the ferromagnetic case above, J' is the exchange term, S is the angular momentum and the constant S_{af}, which depends on the crystal and magnetic structure, has been calculated for several types of lattice [24, 23]. Therefore the total heat capacity in the low-T limit would be

$$C_v = \gamma T + \beta T^3 + \delta T^{3/2} + \eta T^3. \tag{2.14}$$

But note that at least one of the two terms δ and η would be zero.

One of the challenges to analyzing the heat capacity data for magnetic materials is to separate the magnetic contribution. The entropy provides a quantitative comparison which helps to do this. By integrating the measured heat capacity we obtain the change in entropy,

$$S_e = \int \frac{C_v}{T} dT. \tag{2.15}$$

For rare-earth atoms acting as weakly-interacting local moments, each particle has an intrinsic total angular momentum J, and the ground state will be $2J + 1$ fold degenerate. At high temperatures all these states are populated, and hence the

magnetic entropy should saturate to,

$$S_c = R\ln(2J + 1), \tag{2.16}$$

where J the total angular momentum By comparing the experimental (S_e) and calculated (S_c) entropy one can get an idea about the degeneracy of the system and the J value. For most of the materials I studied, entropy saturation could be observed and compared to (2.16).

The temperature at which S saturates gives information about crystalline electric fields (CEFs). The $2J + 1$ levels will be split in the presence of CEFs, with energy level splittings usually on the order of hundreds of kelvin, and the magnetic ordering transition temperature is on the order of tens of kelvin.

D.   Schottky Anomaly

One of the important properties of rare-earth metals is the relative insensitivity of unfilled $4f$ electrons to the local environment. $5d$ and $6s$ electrons form itinerant electron bands in metallic solids whereas the $4f$ electrons tend to remain localized with negligible overlap with neighboring ions. However in some situations, there can be polarization of band electrons through exchange interactions with the $4f$ electrons, which can affect the local moments and lead to anomalies in ordered systems [26, 27]. Typically when the temperature increases from 0 K, the internal energy of the system increases rapidly as the CEF-split levels become populated, hence there can be a large contribution to the heat capacity. CEF Schottky anomalies can then be observed in the paramagnetic phase in addition to strong anomalies due to phase transitions to ordered magnetic states. The specific heat anomalies I have observed are very sensitive to the spacing and degeneracy of quantized energy levels. Here I will consider the

simplest case, a two level system, and give a theoretical framework and show how these anomalies are sensitive to degeneracy and spacing of CEF levels. Consider two levels, a ground state with energy $\epsilon_0 = 0$ and degeneracy g_0 and a first excited state with energy ϵ_1 and degeneracy g_1. Therefore the average energy of an N particle system is

$$E = \frac{N g_1 \epsilon_1 e^{-\epsilon_1/kT}}{g_0 + g_1 e^{-\epsilon_1/kT}}, \tag{2.17}$$

hence the magnetic Schottky heat capacity is

$$C_{Sch} = \frac{\partial E}{\partial T} = N k \left(\frac{\epsilon_1}{T}\right)^2 \frac{g_0}{g_1} \frac{e^{\epsilon_1/k_B T}}{(1 + \frac{g_0}{g_1} e^{\epsilon_1/k_B T})^2}. \tag{2.18}$$

If the energy separation is expressed in terms of $\delta = \epsilon_1/k_B$ measured in temperature units, where $N_A k_B = R$, the Schottky heat capacity per mole of rare earth atoms is reduced to

$$C_{Sch} = \frac{\partial E}{\partial T} = R \left(\frac{\delta}{T}\right)^2 \frac{g_0}{g_1} \frac{e^{\delta/T}}{(1 + \frac{g_0}{g_1} e^{\delta/T})^2}, \tag{2.19}$$

and the limiting high-T entropy is

$$S_{Sch} = \int_0^\infty \frac{C_{Sch}}{T} dT = R \ln(\Omega), \tag{2.20}$$

Where $\Omega = $ total number of states. The resulting C_{Sch} for a two level system is plotted in Fig. 5. The peak in this plot is known as a Schottky anomaly. Different peak shapes correspond to different possible degeneracies of the two states. At $T >> \delta$, C_{Sch} approaches a $1/T^2$ behavior.

E.   Heat Capacity at T_c

In addition to CEF Schottky anomalies, heat capacity features can also signal magnetic transitions at low temperatures. The corresponding heat capacity jump at T_c can be estimated using molecular mean field theory, in which the exchange interac-
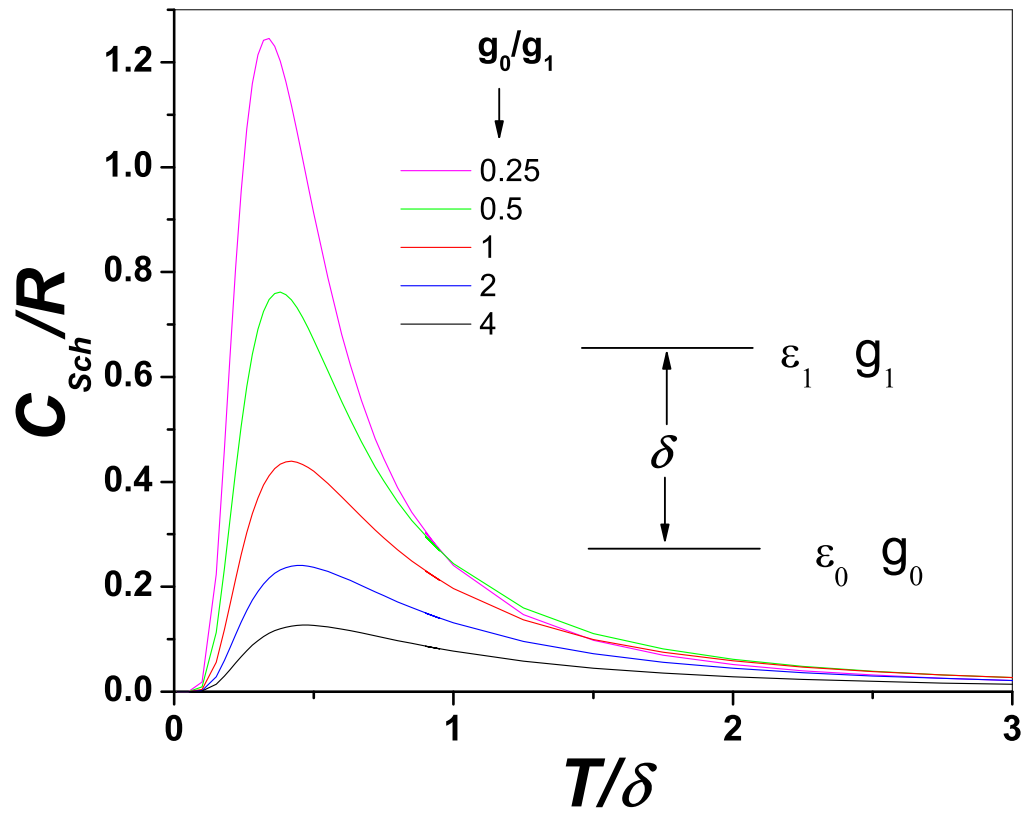
Fig. 5. The Schottky heat capacity of a two level system. Different curves represent different degeneracies of these levels.

tion may be viewed as an interaction between the magnetic moment of the ion and an effective field produced by the rest of the spins in the crystal [23]. Hence the corresponding heat capacity jump at T_c is

$$\Delta C_M = 5R \frac{J(J+1)}{(J+1)^2 + J^2}. \tag{2.21}$$

CHAPTER III

MAGNETISM

In this chapter I introduce some magnetism basics relevant to my work. This will include Hund's rules, different types of magnetic order, the Curie-Weiss law, meta-magnetic transitions and the Brillouin function.

A.   Magnetic Moment

A fundamental quantity in magnetism is the magnetic moment defined as $\mu = \gamma J$, where γ is the gyromagnetic ratio. The magnetic moment is measured in the units of Bohr magnetons (μ_B):

$$\mu_B = \frac{e\hbar}{2m_e} = 9.27 \times 10^{-24} \text{A.m}^2. \tag{3.1}$$

B.   Angular Momentum

To describe the origin of magnetism, one has to consider the orbital motions and spin motions of electrons and the interaction between them. The total orbital angular momentum of a given atom can be defined as

$$L = \sum_i l_i, \tag{3.2}$$

While the total spin angular momentum of a given atom is defined as

$$S = \sum_i s_i, \tag{3.3}$$

where i counts the electron in an incomplete shell and l_i and s_i are the orbital and spin angular momentum of i'th electron. L and S combine to form a total angular

momentum J. The quantum number in the case of spin-orbit-coupled ions is

$$J = L \pm S, \tag{3.4}$$

according to the rules defined below.

C.   Hund's Rules

Hund's rules predict the ground state magnetic configuration. Under the conditions relevant to this work, the magnetic moment of an ion can be estimated assuming that only the ground state is populated. In such cases Hund's rules predict the values for L, S and J. These values are as follows:

Rule 1 & 2: Arrange the electrons so as to first maximize S, and then further to maximize L.

Rule 3: The value of J is $L - S$ if the shell is less than half full and $L + S$ if it is more than half full.

For a given atom, one normally knows the number of outer shell electrons. For example Nd^{3+} has three outer shell $4f$ electrons. f electrons have $l = 3$ and $m_l = -3$ to $+3$, for a total of $2l + 1 = 7$ orbitals. 3 f shell electrons will occupy the $m_l = -3, -2$ and -1 states each with spin up. This implies $L = | - 3 - 2 - 1| = 6$ and $S = 1/2 + 1/2 + 1/2 = 3/2$ and therefore $J = L - S = 9/2$ since the ion is less than half full. This ground state can be denoted by $^{2S+1}L_J =^4 I_{9/2}$.

Since Hund's rules predict the ground state, the magnetic moment of an ion can be estimated assuming that only this ground state is populated. At high temperatures in the paramagnetic region the effective magnetic moment is [6]

$$\mu_{eff} = p_{eff}\mu_B = g_J\sqrt{J(J+1)}\mu_B \tag{3.5}$$

where

$$g_J = \frac{3}{2} + \frac{S(S+1) - L(L+1)}{2J(J+1)}, \tag{3.6}$$

with g_J called the Lande g-factor. For the above example of Nd^{3+}, $p_{eff} = 3.62$. This value can be compared to the experimental p_{eff}, which can be deduced from M vs. T measurements as described below.

D. Curie Law

The magnetic moment per unit volume is defined as the magnetization (M). In most cases we measure the magnetization as a function of temperature (T) and magnetic field (B). For the case of non-interacting moments the magnetization is

$$M = M_s B_J(y) \tag{3.7}$$

where

$$M_s = n g_J \mu_B J \tag{3.8}$$

and

$$y = \frac{g_J J \mu_B B}{k_B T}, \tag{3.9}$$

and $B_J(y)$ is the Brillouin function, defined as:

$$B_J(y) = \frac{2J+1}{2J} \coth\left(\frac{2J+1}{2J}y\right) - \frac{1}{2J}\coth\left(\frac{y}{2J}\right). \tag{3.10}$$

For the case of small y, or equivalently small B or large T, one can easily establish that

$$B_J(y) = \frac{(J+1)y}{3J} + O(y^3). \tag{3.11}$$

Hence in the high T limit the susceptibility is given by

$$\chi = \frac{M}{H} = \frac{n\mu_0 \mu_{eff}^2}{3k_B T} = \frac{C}{T}, \tag{3.12}$$

with μ_{eff} defined as in (3.5). The above equation demonstrates that the high-T magnetic susceptibility is inversely proportional to temperature, which is known as Curie's law. By fitting of χ vs. T data to Curie's law we can obtain μ_{eff} assuming the density n of paramagnetic moments is known. This can be compared to the calculated μ_{eff} to determine the ground state J value.

E.   Magnetic Ordering Types

So far only noninteracting moment systems have been considered, but when the interactions between moments are included, different types of magnetic ordering can occur. The Curie law is modified, becoming the Curie-Weiss law, which is defined as:

$$\chi \propto \frac{1}{T - \theta},$$ (3.13)

where θ is the Weiss temperature. Depending on the sign and the value of θ, magnetic materials are divided into three types. If $\theta = 0$ the material is paramagnetic, if $\theta > 0$, the material is ferromagnetic, and if $\theta < 0$ the material is antiferromagnetic.

1. Ferromagnetism

In a ferromagnet (FM) all the magnetic moments are in a parallel alignment as T goes to zero. Such a material has a spontaneous magnetization due to the exchange interaction even in the absence of applied field. The low field susceptibility of a ferromagnet is given in equation (3.13). In ferromagnetic materials, θ is positive [28]. Typically it is close to the transition temperature (T_C). In mean field theory the two temperatures are exactly identical, but in real systems they are usually different.

In some materials, the magnetization does not completely saturate at the maximum available field (7 T in our case), because of domain wall effect and it is hard to rotate the magnetization away from easy axis. We use the following formula which accounts for those mechanisms and fit to get the saturation magnetization [29]:

$$M = A - B/H - C/H^2. \tag{3.14}$$

2. Antiferromagnetism

A simple antiferromagnet (AF) consists of two magnetic sub-lattices with opposing magnetization. All moments within each sublattice are aligned with each other; whereas, the two different sub-lattices have magnetization with antiparallel orientations. If the magnetic moments are equal then the total magnetization of the system is zero, which is the AF situation. The Curie law is modified accordingly. Hence the susceptibility of an antiferromagnetic material [28] is

$$\chi \propto \frac{1}{T - \theta} \approx \frac{1}{T + T_N}. \tag{3.15}$$

In antiferromagnetic materials θ is negative, and it is identical to the Neel temperature (T_N) for the simple case of AB sublattices and mean field. But in general θ deviates from T_N.

3. Ferrimagnetism

Ferrimagnets, in contrast to AFs, can have two sub-lattices which are not completely anti-aligned, for example when opposing magnetic moments occupy two kinds of lattice sites with different crystallographic environments, or when opposing ions have different intrinsic moments. Hence there is a small spontaneous magnetization below the ordering temperature. In this case normally θ is negative but not the same as the ferrimagnetic Neel temperature (T_{FN}) [28].

4. Metamagnetic Transitions

In antiferromagnetic materials a sudden change from anti-parallel to parallel sub-lattice magnetization can occur when the applied field is able to overcome the AF coupling between the two sub-lattices. This phenomenon is called a metamagnetic transition. In some cases, these are partial step-wise transitions. In some of the materials I have investigated, this phenomenon is clearly visible in magnetization measurements. In this case the magnetization initially increases with the field slowly while above a certain field it increases suddenly. We investigated this phenomenon by measuring M vs. H at different fixed temperatures.

In addition to the above discussed different types of magnetic structures there are other types of magnetic ordering including spiral and helical structures in which the direction of a magnetic moment precesses in space around a cone, and spin glasses in which the magnetic moments lie in frozen random arrangements [30].

F. Crystalline Electric Field (CEF) Effects

A magnetic ion in a crystal experiences a crystalline electric field produced by surrounding ions and valence electrons. For rare-earth ions this can give rise to a ground

state J-multiplet splitting which might be on the order of 10-20 meV. The degeneracy of this J- state will be further lifted by the presence of a magnetic field as well as the presence of the crystal field. The size and nature of the CEF depends on the crystal structure, symmetry and kind of nearest neighbor ions. The CEF's can dramatically influence the magnetic properties of the corresponding material. The CEF part of the Hamiltonian is given by

$$H_{cf} = \sum_n \sum_m B_n^m O_n^m, \tag{3.16}$$

where the O_n^m are the elements of the Stevens operator which depends on J, and the terms B_n^m are numerical coefficients known as 'crystal field parameters'. In order to obtain the relative CEF energy levels, one has to know the sign and magnitude of the coefficients B_n^m. One of the ways to determine B_n^m is approximately through point charge calculations while the other way is through experimental means by measuring neutron scattering, susceptibility or heat capacity. Point charge calculations are poor approximations, and todays sophisticated computational tools are used to perform these calculations. For example the WIEN2K [31] package used in our lab is able to do this to some extent. In this dissertation, I quantified CEF splittings by measuring the H and T dependence of the heat capacity, fitting of the corresponding Schottky anomalies and comparison to magnetization and entropy results.

CHAPTER IV

EXPERIMENTAL METHODS

My dissertation work included use of several instruments including: arc melting apparatus for sample preparation, Bruker powder X-ray spectrometer for structural characterization, Cameca electron micro-probe (EDS, WDS, BSE) for elemental composition analysis, Quantum Design SQUID magnetometer for magnetization measurements, a Physical Property Measurement System (PPMS) for heat capacity and resistivity measurements, and a solid state NMR spectrometer for probing local magnetic interactions at an atomic level. All of the measurements described here I performed myself at TAMU except that the PPMS system was run by Dr. K. D. D. Rathnayaka. I prepared most of the samples for this work, although I obtained a few of the materials from Dr. Y. Oner, our collaborator in Turkey. Oner also performed resistivity measurements on some of the samples of mutual interest, results which have been included in some of the publications referenced in this dissertation [19, 32].

A.   Sample Preparation

Polycrystalline samples were prepared by an arc melting process. Samples were melted several times starting with the pure metals in the desired ratio in an argon atmosphere, on a water cooled copper crucible. The ingots were re-melted several times to ensure homogeneity, and annealed typically for one month in an evacuated quartz tube. Excess Pb was used to control for the loss of Pb during melting, with weighing and micro-probe measurements used as a check for the final results.

Although there are numerous reports of studies on ternary intermetallics, there has been much more limited study of the Pb based materials. This is in part because of the very high chemical reactivity of these plumbides with air. This

presents a challenge, and it requires special handling when we measure the physical properties. The powder, in particular, is very sensitive to air. Thus powder X-ray requires care because of oxidation issues. I used Mylar tape to protect the sample while the measurement was in process, and prepared the powder in a nitrogen glove bag. Some of these materials are flammable, beyond just as an oxidation problem. When making a powder, these can catch catch fire and ruin the entire sample in a fraction of a second. This has happened, particularly for Ce based materials. To avoid this, I used acetone as a fluid mix. By this method I was able to achieve X-ray powder patterns with few or no extraneous peaks which could be fitted well to the desired structures. Sample storage is also an issue; left outside for a day or two, most of the materials will turn to whitish powder. To avoid this I have stored all of my samples in bulk form in mineral oil to prevent air diffusion and to displace air from, the vial. When the samples are in bulk form, the oxidation issue is not as severe; however, even then I minimized the air exposure time and did all the sample preparation an inert Ar gas atmosphere inside a glove box prior to actual measurements.

B. X-ray

The powder X-ray pattern is a one-dimensional recording of intensities as a function of the angle 2θ. Each peak arises due to reflections from a stack of parallel atomic planes within the crystal that diffract at angle θ. From a knowledge of θ, we can derive the interplanar spacing of the layers using Bragg's law. X-ray diffraction using copper $K\alpha$ radiation was used to determine the crystal structure. For peak search, the TOPAS database software from Bruker, Inc. was used. Refinement was done using the GSAS package [33].

X-ray diffraction provides basic structural information. Following standard pro-

cedure, the samples were ground to fine powder for these measurements using an agate mortar and pestle; this ensures all the orientations are represented in the spectrum. To prevent oxidation, as described above, I ground the sample in acetone and the fluid mix was then cast onto a sample holder and dried slowly. The goal in this case is to produce a very flat layer of sample powder. X-rays scattered from the surface of the sample are measured in the detector. The thinner the sample layer, the more accurate the position of the peaks recorded. The sample holder has a cavity a few mm deep and a circular glass slide sits inside the cavity.

1.   Electron Micro-probe

Microprobe analysis is very useful in the study of minerals, metals and semiconductors because it can give major, minor and trace element compositions very accurately with minimum damage to the sample. The most important type of micro-probe instrument involves the use of an electron beam because of the wealth of information that can be obtained from the interaction of an electron beam with the sample. This helps for characterizing the microstructure and micro-composition of materials. Such a micro-probe instrument includes a scanning electron microscope, electron probe X-ray micro-analyzer (WDS and EDS spectrometers), BSE detector, and optical microscope.

In the electron micro-probe, a high voltage electron beam hits the target material and emits characteristic X-rays which can yield both qualitative identification and quantitative composition from regions of a specimen as small as a micrometer in size. X-ray photons emerging from the specimen have energies specific to each element in the specimen. These characteristic X-rays provide the micro-probe's analytical capabilities.

The Energy Dispersive Spectrometry (EDS) offers a quick identification of ma-

jor and minor elements and helps to set up the needed experimental parameters for Wavelength Dispersive Spectroscopy (WDS) analysis for the elements of interest. Even though EDS can give quantitative analysis, WDS was used to avoid peak overlaps and to get better resolution.

For these measurements, samples were prepared using epoxy, and mechanically polished to a flat surface. After the specimen was embedded into epoxy, it was polished with SiC wet paper. I removed SiC particles before repeating the procedure with finer grain paper and with ultrasonic cleaning between steps. The last polishing step used three micron alumina powder, wetted with water. Samples were carbon coated as a conductive coating. This coating is important because during data collection and imaging, electrons bombarding the specimen could build up a negative charge on areas of the specimen. This charge, if large enough, could deflect both incident and emitted electrons and distort the image. In my samples, this coating also helped to prevent air exposure.

I also used Back Scattering Electron (BSE) images to provide qualitative information about the uniformity and homogeneity of the sample. This helped in indicating the number of phases and number of points to be analyzed by EDS and WDS. Finally, for quantitative analysis, I did WDS measurements using the electron micro-probe to confirm the desired phases and compositions.

2. SQUID

Susceptibility, magnetization, $M - H$ and $M - T$ measurements were done using a Quantum Design MPMS SQUID system. This instrument provides ultra-sensitive measurements over a wide range of temperature and applied magnetic fields. A regular plastic straw was used as a sample holder because it has a low mass and less diamagnetic background signal. The sample was cut into an elongated piece to minimize the demagnetizing fields, and put into a small plastic bag, inserted into a straw. The plastic bag signal was subtracted using the known mass once the measurement was done.

3. PPMS

As discussed in Chapter II the measurement of heat capacity provides much information about lattice, electronic and magnetic properties of materials. A Quantum Design Physical Property Measurement System was used to measure the heat capacity as well as resistivity. This is a commercial device, for which there are different pucks for different measurements. The heat capacity was measured by an adiabatic method in the temperature range from 2 to 300 K. On the specific heat measurement puck, a heater and thermometer are attached to the bottom of a sample platform. Small wires provide the electrical connection to the heater and thermometer and also provide the thermal connection and mechanical support to the sample platform. The sample platform accommodates small samples weighing approximately 100 mg or less. The sample has to be finely polished and shaped to the platform dimensions to make a better thermal contact. I cut and mounted the sample to a glass slide using crystal bond, polishing one side first before mounting. The sample is attached to the platform by a thin layer of Apiezon grease, which provides the required thermal con-

tact. A thermal shield covers the top of the puck, which minimizes extraneous heat input. The grease and sample holder heat capacities, the "addenda", are removed automatically using addenda tables measured previously. Sometimes a peak close to 300 K coming from the Apiezon grease limits the ability to obtain data close to room temperature. Thermal relaxation time constants are on the order of minutes at 300 K. It can thus take a long time to measure one data point as compared to low temperatures. Therefore, although this system can measure from 2 K to 400 K I minimized the number of data points at high temperature. A smaller sample will take less time; however, this is a trade-off since in that case the heat capacity of the grease may dominate.

Resistivity measurements were also done using the PPMS, by a standard four probe method over the temperature range from 2 to 300 K. Electrical contacts were made using silver paint and 25 μm gold wire. I also used a homebuilt liquid helium dipper system for some additional resistivity measurements.

CHAPTER V

EXPERIMENTAL RESULTS AND DISCUSSIONS

A. Nd_2Ni_2Pb

1.   Experimental

Samples of Nd_2Ni_2Pb were prepared by arc melting, starting with the pure metals. Loss of Pb was accounted for by adjusting the starting ratio. Three samples, prepared both at Texas A&M and at Istanbul, showed nearly identical magnetic properties. One of these received a full X-ray and electron micro-probe analysis. Crystal structure information for this sample is reported in reference [9]. The sample was re-melted several times to ensure homogeneity, then annealed at 873 K in an evacuated quartz tube for 30 days. X-ray diffraction was used to determine the crystal structure, with refinement performed using the GSAS package [34]. We used WDS scans to confirm the desired single phase with the 221 composition. Results are shown in Fig. 6. Susceptibility and magnetization measurements were done using the SQUID system. For these measurements the long axis of the sample was along the field direction, minimizing demagnetizing field effects. The temperature dependence of the heat capacity was measured in the temperature range from 2 to 300 K.

2.   Results and Discussion

a.   X-ray

Powder x-ray results for Nd_2Ni_2Pb are shown in Fig. 6. GSAS refinement analysis showed that the main phase is orthorhombic Nd_2Ni_2Pb with $a = 0.4138$ nm, $b = 1.4292$ nm and $c = 0.3750$ nm, in agreement with established lattice parameters [9]. Aside from the majority reflections, two additional peaks were seen, however these
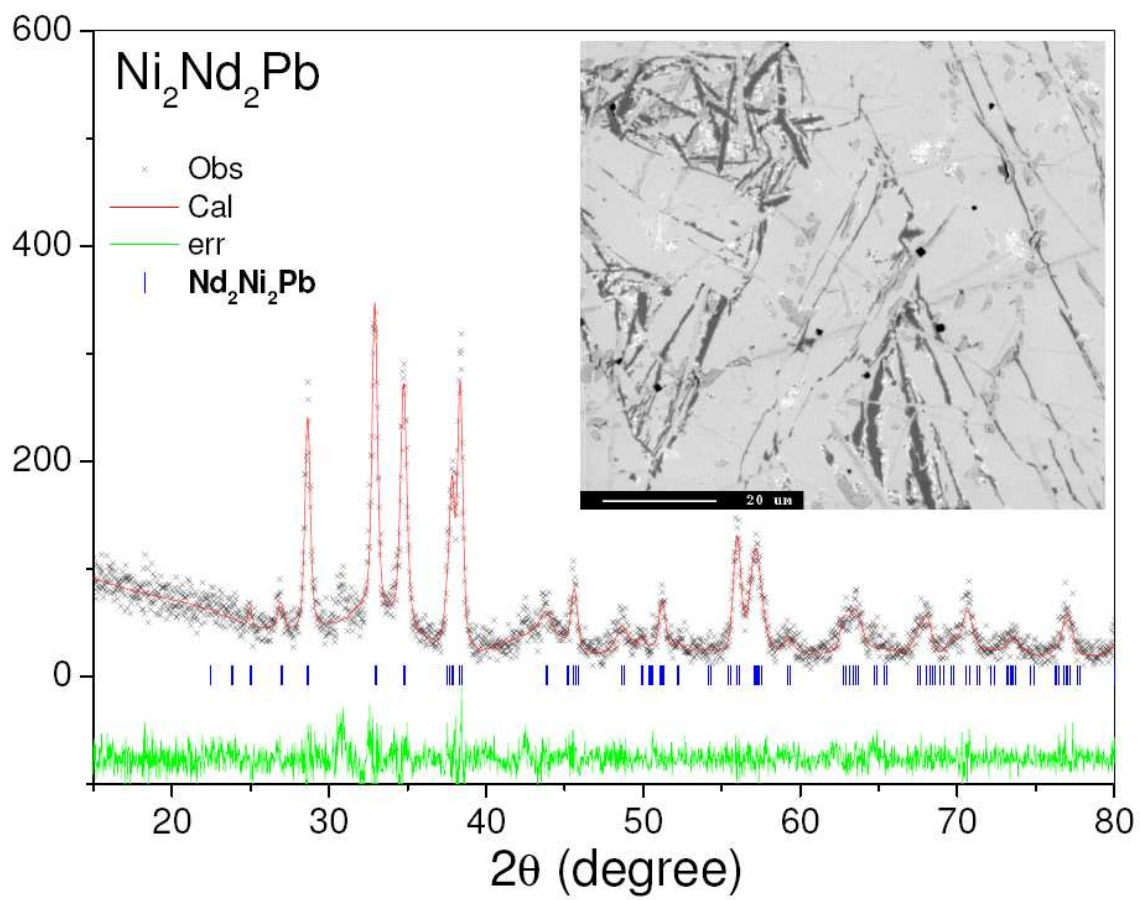
Fig. 6. Powder X-ray results for Nd$_2$Ni$_2$Pb, with results of refinement and difference plot. Vertical marks are fitted reflections. Inset: BSE image of Nd$_2$Ni$_2$Pb. Light gray is the main phase.

were very weak and could not be indexed. There was no evidence for unreacted Pb or NdNiPb (111 phase) in the spectrum. WDS imaging showed a very small amount of the 111 phase, below the X-ray detectability limit, but otherwise these scans confirmed the sample to be nearly pure Nd_2Ni_2Pb.

b. Magnetization

Fig. 7 shows the dc susceptibility measured in a field of 1000 Oe. Anomalies are observed near 80 K and 20 K. A Curie-Weiss fit to the high-temperature data gives the dashed curve in Fig. 7. This yields $p_{eff} = 3.73$, and $\theta = 1.2$ K, with an effective moment close to the free ion moment for Nd^{3+} ($p_{eff} = 3.62$) [6]. This establishes that Nd is in the trivalent state, and Ni is not magnetic as also observed in other R_2Ni_2Pb intermetallics. Below 80 K, the susceptibility deviates from Curie-Weiss behavior, due largely to crystal-field splitting of the $J = 9/2$ Nd levels. We have observed some variability near this temperature for different samples, indicating that there may also be a trace magnetic phase involved. However, the magnetization and specific heat measurements described below make it clear that Nd_2Ni_2Pb itself exhibits only a single magnetic transition, corresponding to the 20 K anomaly in the susceptibility.

Fig. 8 shows the zero-field-cooled and field-cooled magnetization at low temperatures. The development of hysteresis below the 20 K anomaly indicates that this phase has a net moment. However, the associated moment is quite small (0.3 μ_B), as we obtained from fitting M vs. $1/H$ below 3 T to $M = A - B/H - C/H^2$, indicating that this is likely a canted phase. Because of lack of symmetry around the bonds joining rare earth atoms in this structure, the Dzyaloshinsky-Moriya mechanism may drive parasitic ferromagnetism in a nominally-antiferromagnetic system [29], likely explaining this behavior. In order to obtain more insight into the magnetic behavior, we carried out $M - H$ measurements. These are shown in Fig. 9. At 2 K a meta-
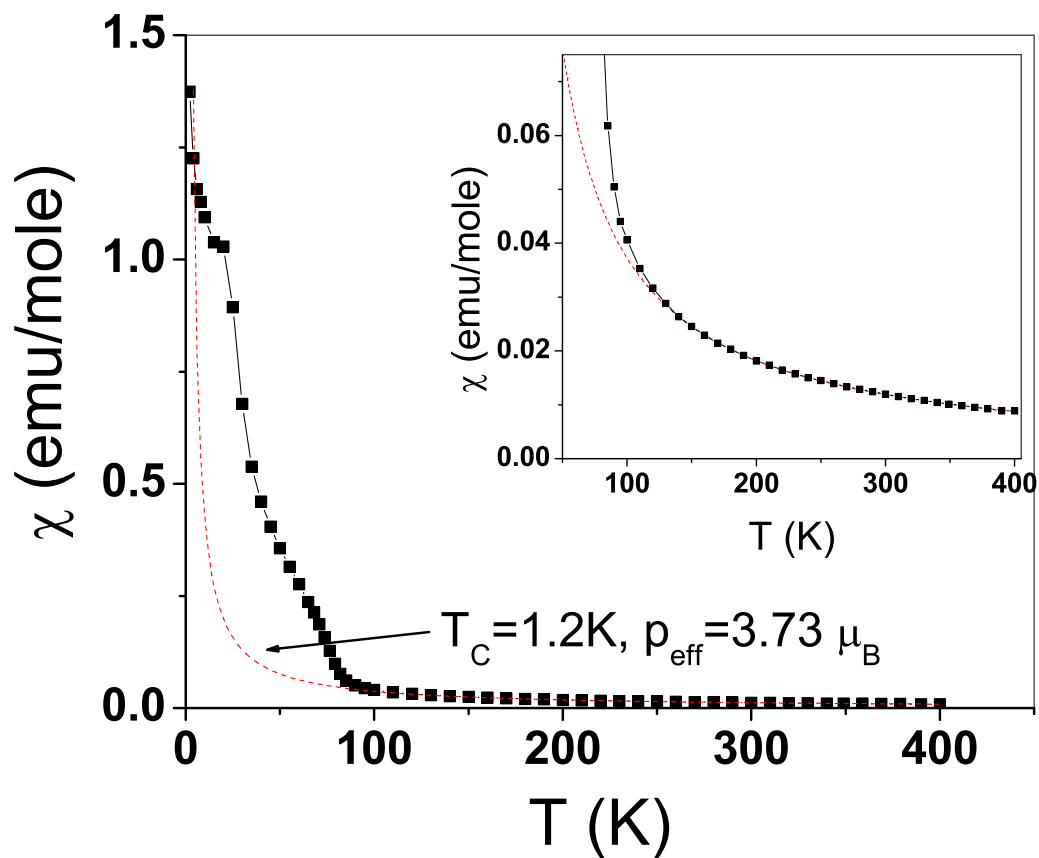
Fig. 7. Nd$_2$Ni$_2$Pb magnetic susceptibility measured in a field of 1 kOe, from 1.8 K to 400 K. Inset: High temperature data. Dashed curve in both plots is a fit to Curie-Weiss law.
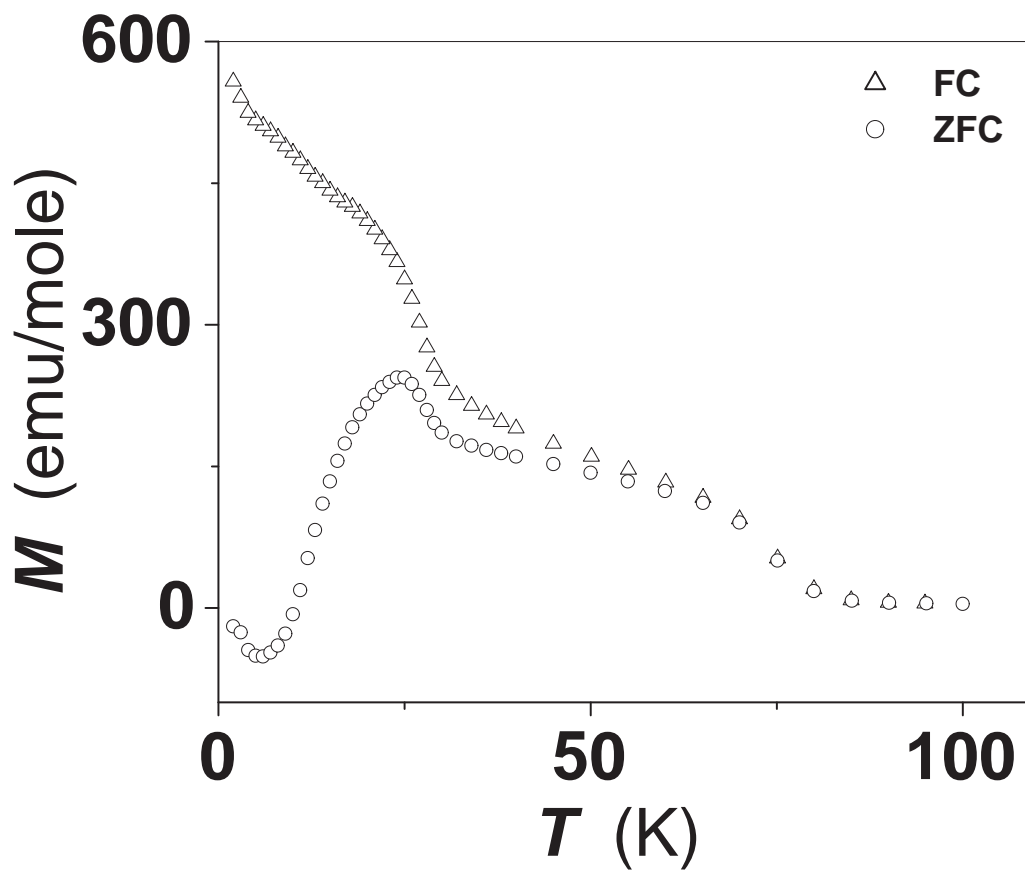
Fig. 8. Zero-field-cooled and field-cooled magnetization for Nd_2Ni_2Pb, showing irreversibility at low temperatures. Measuring and cooling fields 50 Oe.
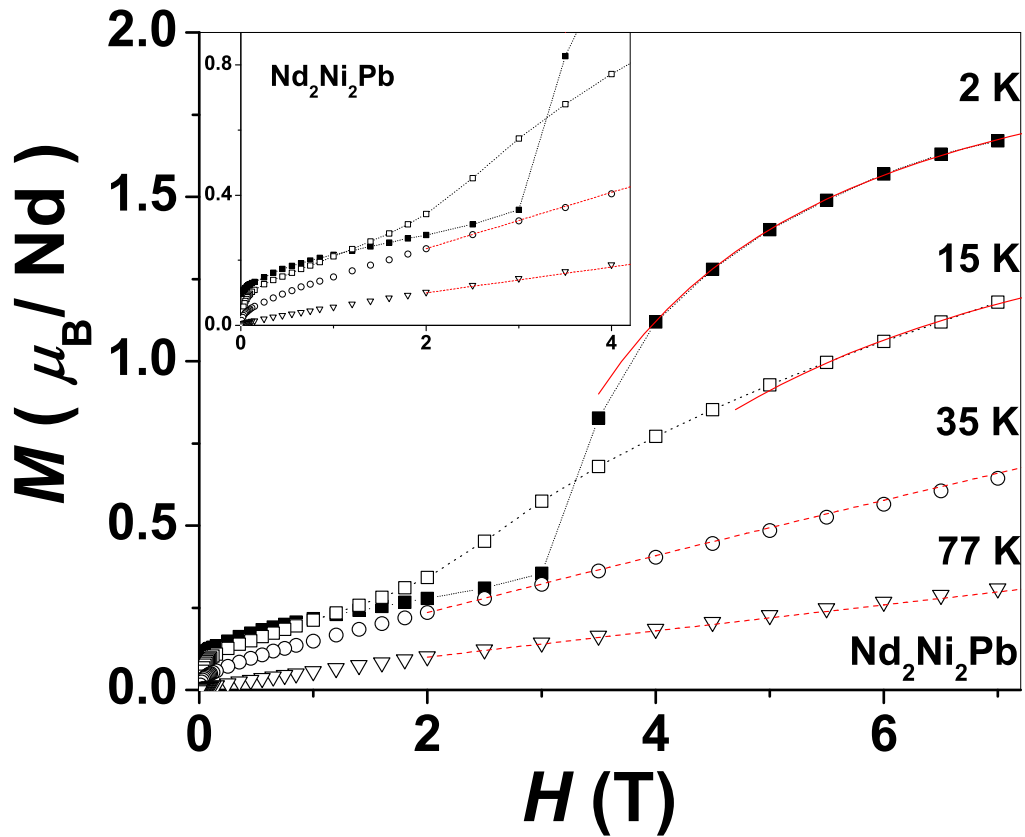
Fig. 9. $M - H$ curve for Nd₂Ni₂Pb measured in fields up to 7 T, at the four temperatures illustrated. Solid curves: saturation fit described in text. Dashed curves: Brillouin fits for 35 K and 77 K, showing paramagnetic behavior. Dotted curves for 2 K and 15 K data are guides to the eye. Inset: An expanded view at low H.

magnetic transition is seen at 3 T with large increase in magnetization. The inset of Fig. 9 shows a clear meta-magnetic transition; saturation at low fields can be seen, which shows that the ground state has a small moment corresponding to a canted phase. At 15 K the corresponding transition occurs at 1.5 T. Fig. 10 shows a M vs. $1/H$ plot for Nd_2Ni_2Pb. A fit to the 2 K saturation behavior, using a function of the form $M = A - B/H - C/H^2$ [29], yielded a saturation magnetization corresponding to 2.1 μ_B per Nd. The fitted curve is also shown in Fig. 9, along with a similar fitted curve for 15 K. This saturation value is smaller than the free ion moment of Nd, $gJ = 3.27$. However it is consistent with the range of values expected for a crystal-field-split ground-state doublet for orthorhombic Nd_2Ni_2Pb. The saturation magnetization for the unsplit moment would be $M_{sat}/\mu_B = gJ = \frac{8}{11} \times \frac{9}{2} = 3.27$. The measured value is a bit different from the closest doublet, $m_J = \pm\frac{5}{2}$, which would have $gJ = 1.82$. This is because of the CEF Hamiltonian, for which B_m^n, O_m^n can give a mixture of levels. Assuming this to be the case, we plotted Brillouin functions in Fig. 9 corresponding to one 2.1 μ_B doublet per Nd, for 35 K and 77 K. The result is in good agreement with the paramagnetic response at those temperatures. This is a strong indication that the observed meta-magnetic transition corresponds to full alignment of such a crystal-field-split doublet, rather than a transition to a new canted state. Thus, the magnetic behavior can be characterized by a single antiferromagnetic phase (with accompanying parasitic ferromagnetism as described above), having T_N=19 K, while the aligned phase is an extension of the paramagnetic phase. The single magnetic phase above the meta-magnetic transition observed here stands in contrast to the multiple magnetic phase transitions, and more complicated spin structures, for the heavier-rare-earth analogs of Nd_2Ni_2Pb [3, 10]. This could be due to Nd being the lightest rare-earth to form a 221 structure, since the larger lattice parameter can affect the RKKY spatial dependence.
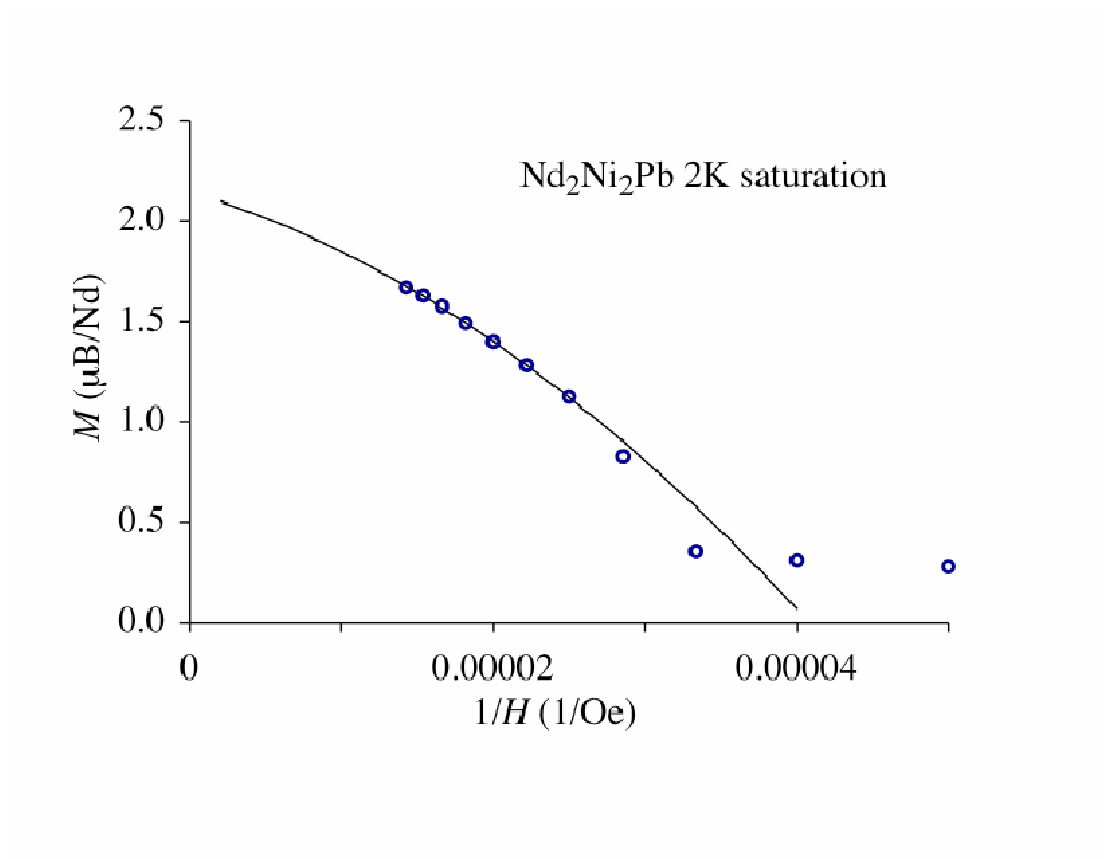
Fig. 10. M vs. $1/H$ for Nd_2Ni_2Pb, and the fitted curve yielding the saturation moment. Details given in the text.

c.   Heat Capacity

Fig. 11 shows the temperature dependence of the heat capacity. At 19.5 K there is a sharp singularity indicative of a cooperative phase transition. The specific heat jump at $T = T_c$ was found to be ΔC_{exp}=19 J/mole-K. This was done by extrapolation, as shown in the figure. The theoretical specific heat jump at the transition temperature can be calculated from simple molecular field theory [25, 23] to yield $\Delta C = 25$ J/K per mole formula unit, assuming that each spin is constrained to a pair of ground-state levels corresponding to an effective spin-1/2. Such an effective spin-1/2 would be equivalent to the doublet state identified from magnetization measurements, as described above. The observed 19 J/mole-K is consistent with the calculated value if a reduction due to critical fluctuations above T_c is taken into account. As $\Delta C = 5R\frac{J(J+1)}{(J+1)^2+J^2}$, if the spins were not in a doublet state, the heat capacity jump would be larger, thus further from the observed value. Below T_c, a fit of the form $\gamma T + \beta T^3$ provides very good agreement with the T-dependent heat capacity, as shown in Fig. 12. The resulting γ value is 8.52 (mJ/mole-K^2). The T^3 term is a characteristic signature of an antiferromagnetic phase [23]; in this case β contains both magnetic and phonon contributions, which are difficult to separate without further information on the magnitude of the phonon component. However, $\Delta S = \int (C/T)dT$, the total entropy change, can provide an upper bound on the magnetic contribution. The value thus obtained below T_c is ΔS= 16.5 J/mol-K, which can be compared to $\Delta S = 2R$ $\ln(2J+1) = 11.5$ J/mol-K for a magnetic disordering transition, for 2 Nd per formula unit, with the effective spin assumed to be $J = 1/2$. This would apply for the case of a doublet even if the magnetic levels do not correspond to the situation $m_J = \pm\frac{1}{2}$. A phonon contribution corresponding to the difference between these values is quite reasonable. On the other hand, ground-state multiplets corresponding to $J = 1$ or
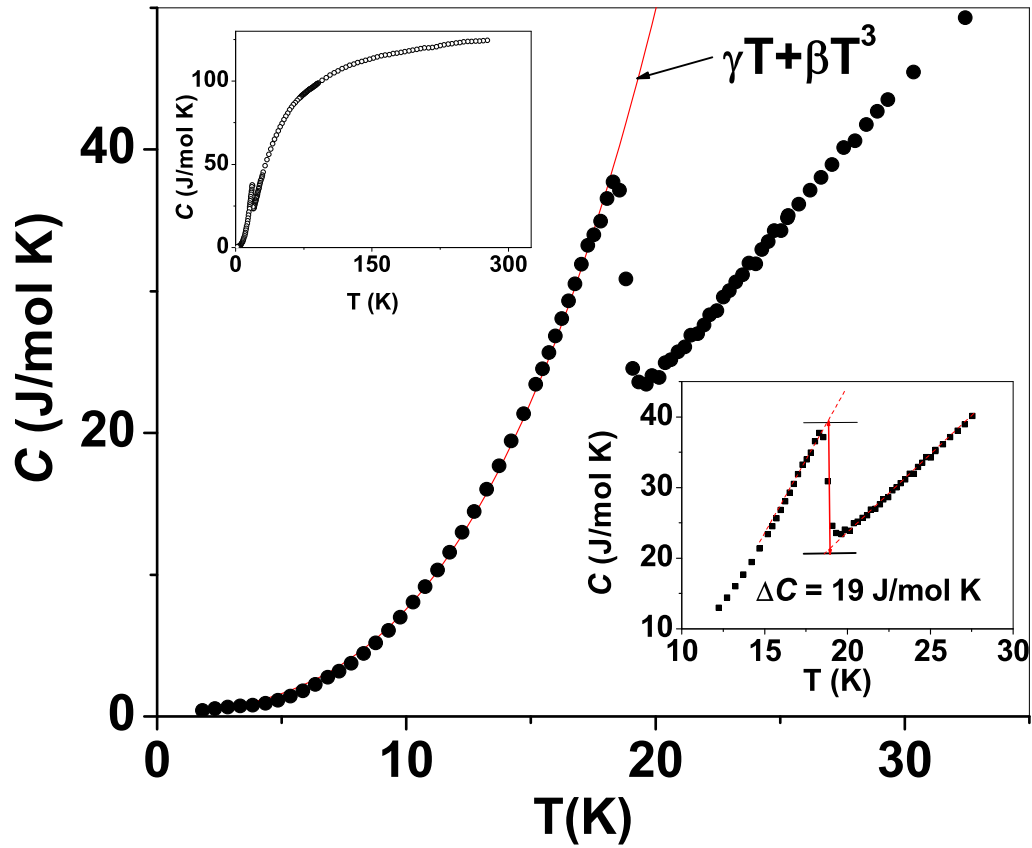
Fig. 11. Low temperature heat capacity of Nd_2Ni_2Pb. Solid curve is the fit described in text. Upper inset: Heat capacity from 2 K to 300 K approaches classical saturated value of 125 J/mol K = $3R$ per atom. Lower inset: specific heat jump at 19 K magnetic transition.
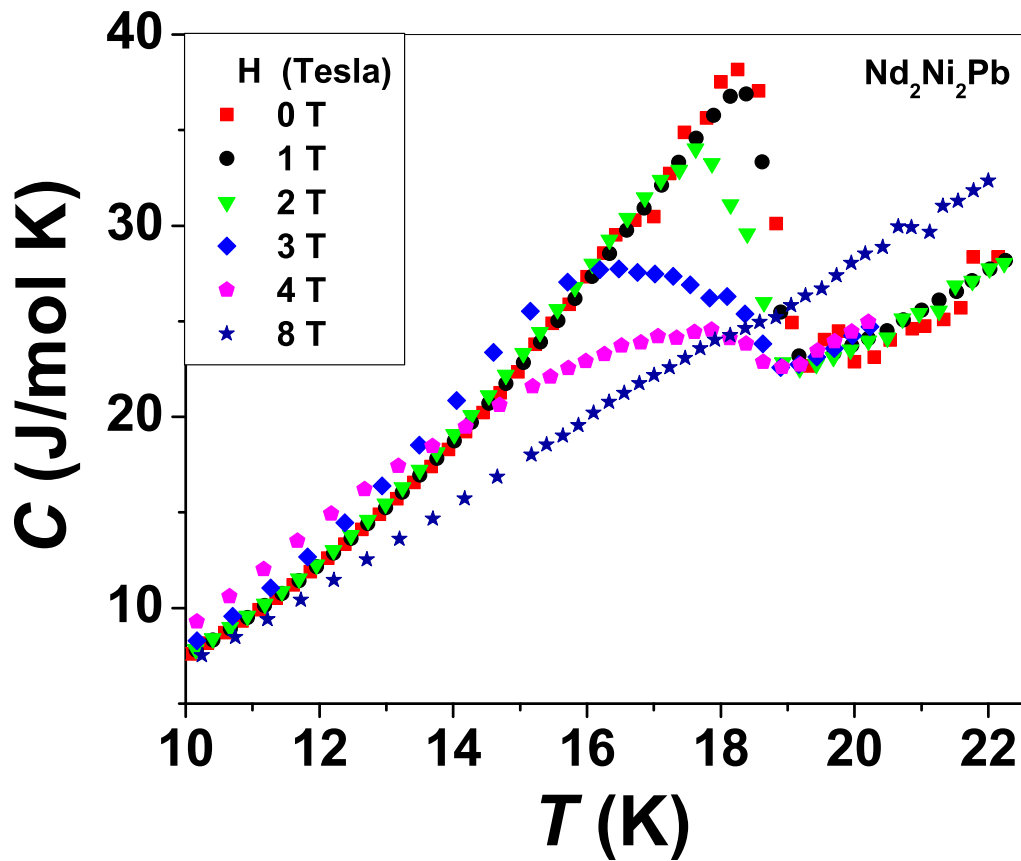
Fig. 12. Field dependent heat capacity of Nd_2Ni_2Pb shows gradual broadening of 19 K transition, which disappears at a field of 8 T.

greater would give $\Delta S = 18.24$ J/mol-K or larger, which is too large to be consistent with the observed entropy change. These results reinforce the conclusion obtained from magnetic measurements, indicating that Nd_2Ni_2Pb exhibits a single magnetic transition having largely antiferromagnetic character, and show that the entire sample contributes to this transition.

d. Resistivity

Fig. 13 shows the resistivity at low temperature for Nd_2Ni_2Pb. It shows a sharp knee at 19 K indicating the magnetic phase transition, which is consistent with heat capacity and magnetization results. Below T_C, a typical spin-scattering behavior is observed, in the ordered state. Below the transition temperature the resistivity is reduced sharply because the scattering is reduced as the spontaneous magnetization increases. This is a very common behavior in magnetic metals. At high temperatures, the results shows metallic behavior, resistivity linear in T.

3. Conclusions

I measured heat capacity, magnetization and dc-susceptibility for Nd_2Ni_2Pb. The heat capacity measurements indicate an antiferromagnetic phase transition at 19 K involving crystal-field-split levels. Magnetization measurements confirm this assignment, and reveal a spin-alignment meta-magnetic transition at 3 T. Observation of a single antiferromagnetic phase differs from the observed behavior of the heavier-rare-earth R_2Ni_2Pb materials.

B. NdNiPb

The NdNiPb (sample NdNiPb-A) sample which I made in summer of 2003 showed apparent partial loss of resistivity near 5 K. However there was no complete transition to zero resistivity, and no apparent Meissner effect. By comparison, earlier samples from Y. Oner exhibited real zero resistance below 6K, which could sustain a relatively large current. WDS measurements on my sample NdNiPb-A showed no unreacted Pb, but there was some fraction of the 221 phase, Nd_2Ni_2Pb. The percentage of 221 was 5-8 % based on an approximate WDS area analysis, while the remainder was 111
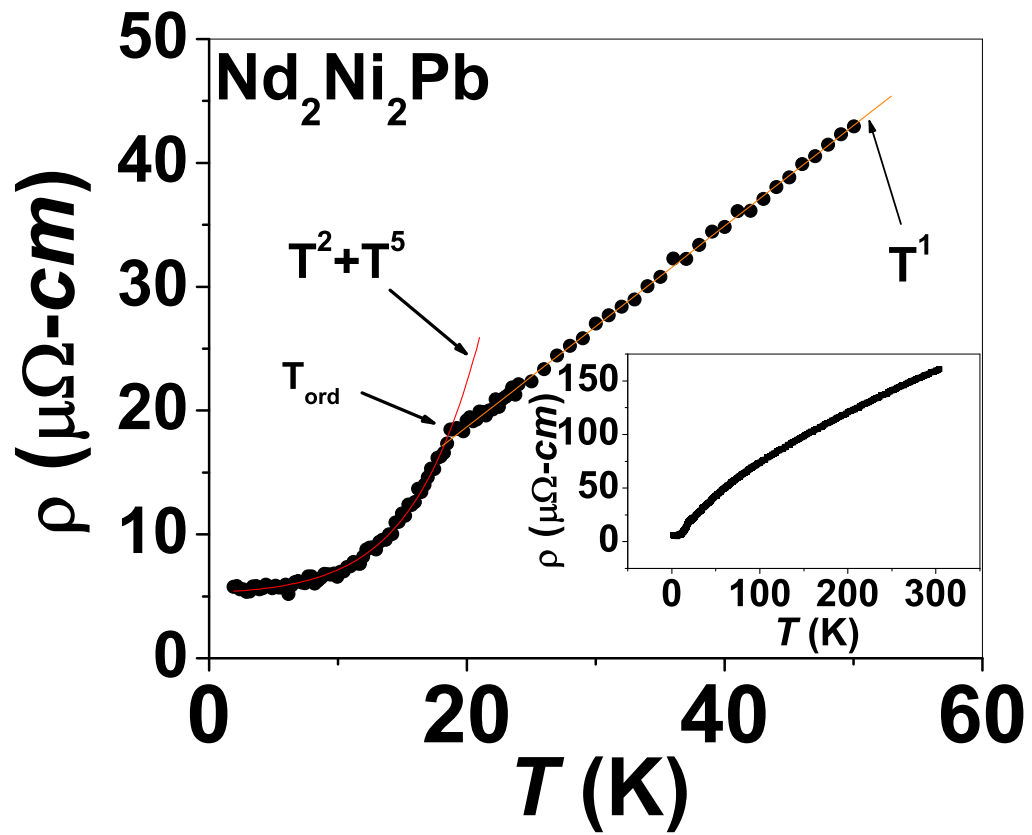
Fig. 13. Resistivity for Nd$_2$Ni$_2$Pb, showing a sharp knee at 19 K indicating the magnetic phase transition.

phase. The structure was not confirmed by X-rays, but clearly a large portion had the 111 composition as seen in WDS. This result rules out superconductivity in the 111 phase. I followed these measurements with an investigation of the 221 phase, as described in the last section, and also with studies of additional single phase samples of NdNiPb, as described below.

1. Experimental

All samples of NdNiPb and YNiPb were prepared by arc melting. Ingots were re-melted several times and annealed at 600 °C for four weeks. The structure was analyzed by X-ray diffraction. After adjustment for loss of Pb, I produced NdNiPb and YNiPb samples that were found to be single phase with the TiNiSi structure type (space group #62: *Pnma*, Pearson code oP12). Crystal structure parameters for all samples were consistent with reported values [8, 9]. A SQUID magnetometer was used to measure DC magnetization with the field along the long axis of the sample to minimize the demagnetizing field. The heat capacity was measured using a Quantum Design PPMS system.

2. Results and Discussion

The initial motivation behind studying this sample was the possible coexistence of superconductivity and antiferromagnetism. In preliminary studies of this material in our laboratory, superconductivity was observed at about 6 K, below an observed magnetic transition. As introduced above, my studies demonstrated that this is not due to NdNiPb, and may be due to an alternative phase. To investigate this we made sevaral batches of NdNiPb samples.

Since resistivity indicated that some small portion of the first sample was super-conducting, initially we guessed that the 221 phase might be superconducting. Later

study of the 221 phase discussed in the previous section showed no apparent super-conductivity. Sample NdNiPb-A was Pb-poor, and no free Pb was seen in WDS, thus the superconductivity probably does not result from elemental Pb. Instead it could be that there is a third unknown phase that superconducts, or conceivably regions of 111 or 221 phase that are off stoichiometry may superconduct. Unfortunately we have not identified the source. Measurements last year in Istanbul confirm that NdNiPb itself is not a superconductor [35].

Sample NdNiPb-B was designed with excess Pb to yield a sample very close to the 111 stoichiometry, and made with higher-purity Nd, to eliminate any spurious composition effects. X-ray powder diffraction showed the 111 phase. No Meissner effect was seen in measurements to 2 K, in a field of 10 Oe. At lower tempera-tures only a susceptibility peak at 4 K indicating a magnetic transition, rather than superconductivity, was observed.

To further understand the magnetic behavior, I measured magnetic, thermal and transport properties of NdNiPb and examined the magnetic ordering and crystalline electric field splitting effects. The properties of NdNiPb were not previously known, although the properties of the other RNiPb compounds have been reported elsewhere [36]. I find that NdNiPb exhibits an antiferromagnetic phase transition at 3.5 K associated with the alignment of crystal-field-split levels of the magnetic Nd ion, and has transport properties close to those of a classic metallic system.

a. Heat Capacity

Fig. 14 shows heat capacity results for NdNiPb and nonmagnetic YNiPb. At high temperatures the heat capacity curves for all samples approach the classical value $3R \times N$, due to vibrational modes as expected. The YNiPb specific heat varies monotonically, with no anomaly down to 1.8 K. Below 6 K the data could be fitted
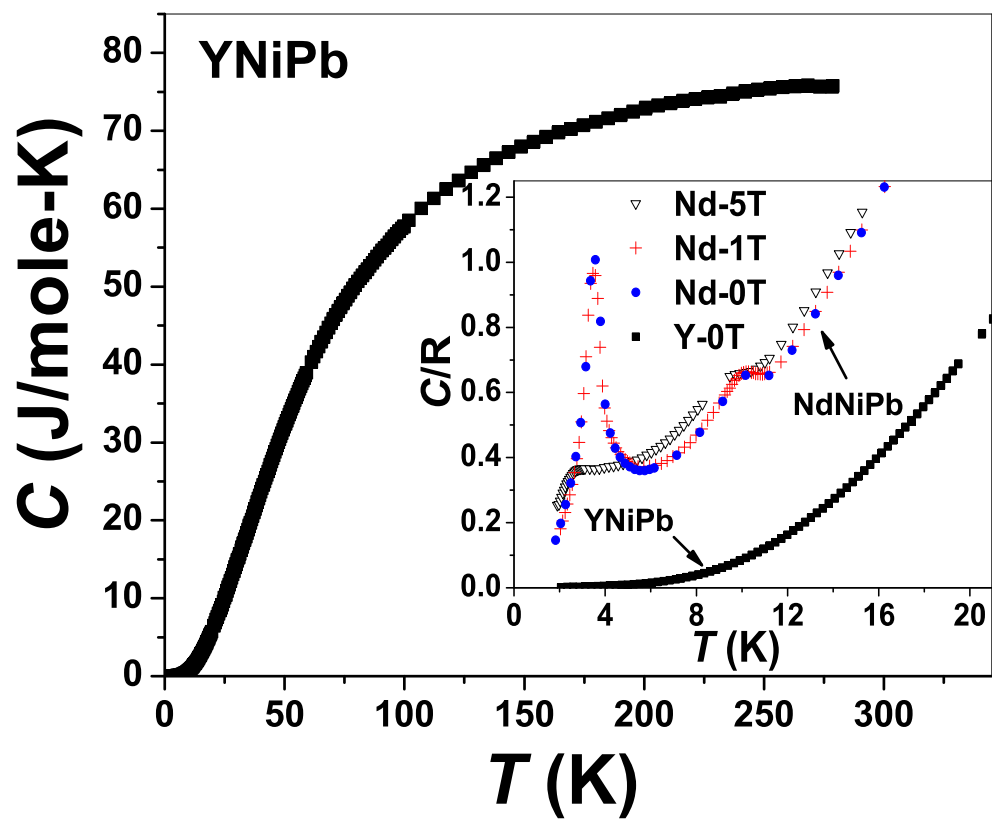
Fig. 14. Specific heat for nonmagnetic YNiPb. Inset: Low temperature specific heat for NdNiPb at different applied magnetic fields, compared to YNiPb.

to $C = \gamma T + \beta T^3$, with $\gamma = 5.26$ mJ/(mole K^2), and β corresponding to a Debye temperature equal to 166 K. The γ value is small and typical of a normal metal. The NdNiPb heat capacity shows a clear sharp peak at 3.5 K (Fig. 14, inset). In larger fields the peak moves to lower temperatures, signaling an antiferromagnetic transition. The difference between the NdNiPb and YNiPb curves at higher temperatures can be attributed to the effect of crystalline electric field (CEF) splitting of the Nd magnetic levels. The low temperature specific heat follows a linear T-dependence. Fitting yielded a large γ of 180 mJ/mol-K^2. This large value is clearly of magnetic origin, and could be due to spin fluctuations extending over a large temperature range. From the entropy analysis the small peak near 10 K can be seen to be a minor second phase.

I isolated the magnetic contribution to the specific heat (ΔC_{mag}) by subtracting the YNiPb curve from that of NdNiPb. Temperatures were scaled proportional to the ratio of molar masses. The result is shown in Fig. 15. Above the low-temperature magnetic transition region a Schottky-like anomaly is seen, due to the freezing out of CEF-split magnetic levels. The J = 9/2 Nd^{3+} levels in NdNiPb may be split into 5 separate Kramers doublets [37], so I derived a corresponding theoretical expression, allowing the energies of the 5 doublets to vary arbitrarily in a least-squares fit above 17 K. This provided an excellent fit to the data, as shown in the main plot of Fig. 15. The result, with levels shown schematically in Fig. 15, corresponds to a doubly degenerate ground-state with a further doublet at 33 K and 6 levels at 96 K, relative to the ground state. The fit is not particularly sensitive to the position of the upper 6 levels.

From (ΔC_{mag}) we obtained the magnetic entropy using $S_{mag} = \int (\Delta C_{mag}/T) dT$. S_{mag} reaches a plateau at high temperatures, very close to the total magnetic entropy $S/R = \ln(2J+1) = 2.30$ for $J = 9/2$ which is shown in Fig. 16. This result is consistent with the expected $J = 9/2$ state for trivalent Nd, and it provides additional confidence in the subtraction of the lattice and electronic parts of C. S_{mag} has its largest drop
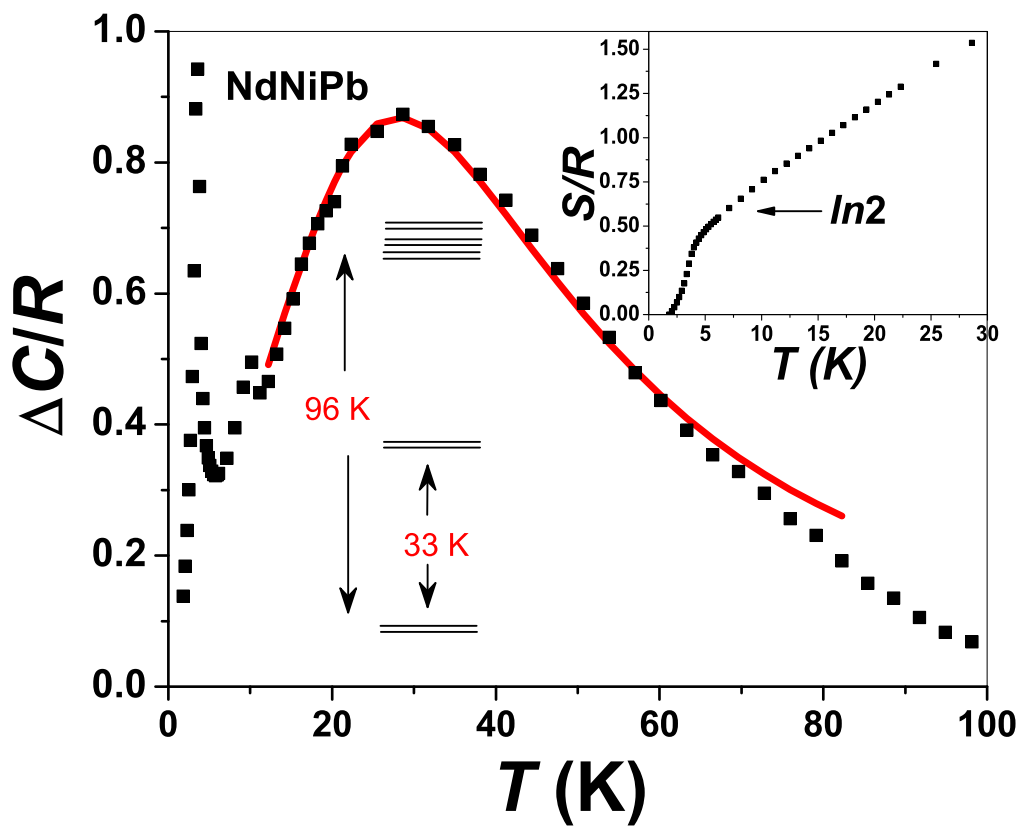
Fig. 15. Magnetic contribution to the heat capacity of NdNiPb at zero field. Solid curve: Schottky-anomaly fit for crystal-field-split levels as described in the text, with splitting shown schematically below the data. Inset: entropy versus temperature, with magnetic doublet value (ln 2) indicated.
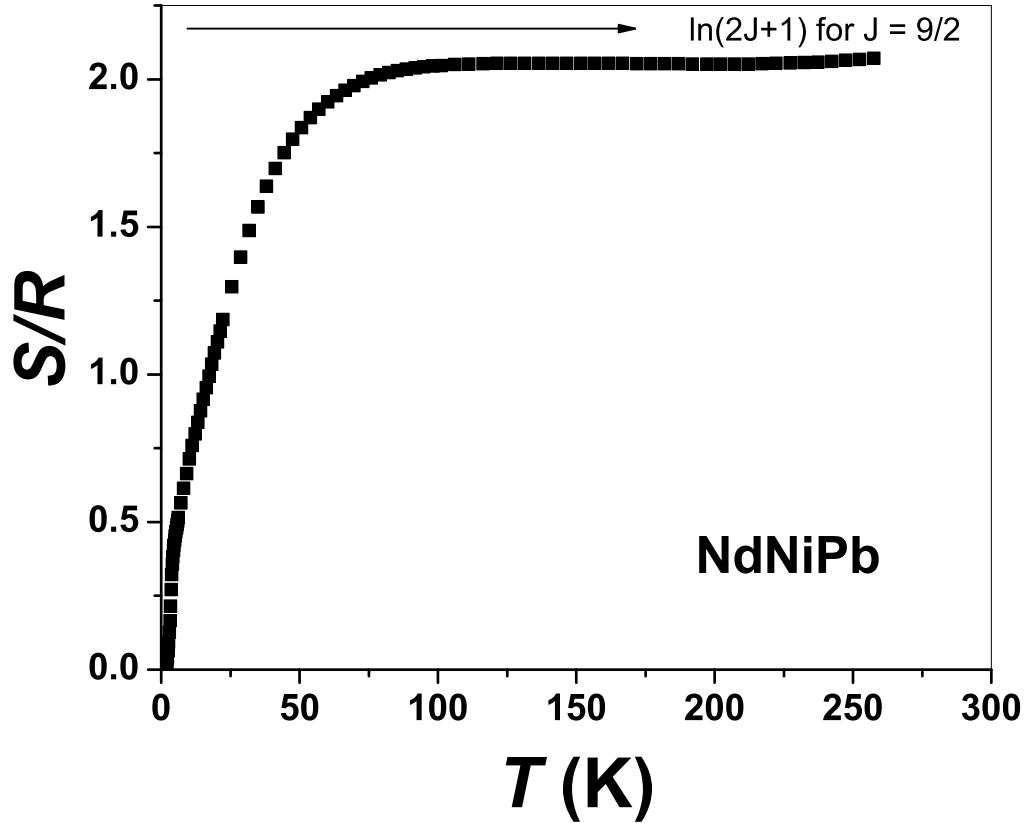
Fig. 16. Magnetic contribution to the entropy versus temperature of NdNiPb with magnetic doublet value (ln 10) for $J = 9/2$ indicated.

over the temperature range corresponding to the Schottky-like peak in ΔC_{mag} due to CEF splitting, while a further drop is observed near T_N. The drop in entropy near T_N is close to that expected for a two-level ground state, although the theoretical value $\Delta S/R = \ln(2) = 0.69$ is not reached until a temperature of 7 K, corresponding to the extent of the visible tail in Fig. 15.

Similarly, the jump in ΔC_{mag} at T_N is smaller than the value $1.5R$ expected for a two-level ground state [23]. The value of ΔC_{mag} is approximately $(1\ R)$ as can be deduced from the data in Fig. 14. Although fluctuations will normally reduce this value,

the present result is considerably smaller that observed, for example in Nd_2Ni_2Pb as described above or a series of commensurate-antiferromagnetic Gd compounds [38]. It may be that the one dimensional nature of NdNiPb leads itself to a greater density of fluctuations.

b.   Magnetic Measurements

Magnetization results for NdNiPb are shown in Fig. 17. A high-T Curie fit yields an effective moment $p_{eff} = 3.59$, very close to the expected Nd^{3+} value of 3.62 [6] indicating that the $3d$ electrons of Ni have no localized moments. The fit has $\theta_p = -26$ K indicating an antiferromagnetic tendency. The peak at 3.5 K is consistent with the specific heat, and is similar to the sharp transition observed in Nd_2Ni_2Pb [12]. M-H measurements at 2 K show little hysteresis, thus the transition is presumably antiferromagnetic, consistent with the specific heat results. This is similar to results for the Gd, Tb, and Dy 111 materials [36].

c.   Resistivity

I also measured the resistivity, which has a metallic temperature dependence for NdNiPb. A sharp drop near 5 K was observed, corresponding to the reduction of spin-disorder scattering at the magnetic transitions. As mentioned above, one of the NdNiPb samples showed an apparent partial loss of resistivity near 5 K. However there was no complete transition to zero resistivity, and no complete Meissner effect.

3.   Conclusions

In summary I report susceptibility, heat capacity and electrical resistivity measurements on recently discovered NdNiPb. A clear phase transition was found near 3.5 K however no superconductivity. With a combination of specific heat and magnetiza-
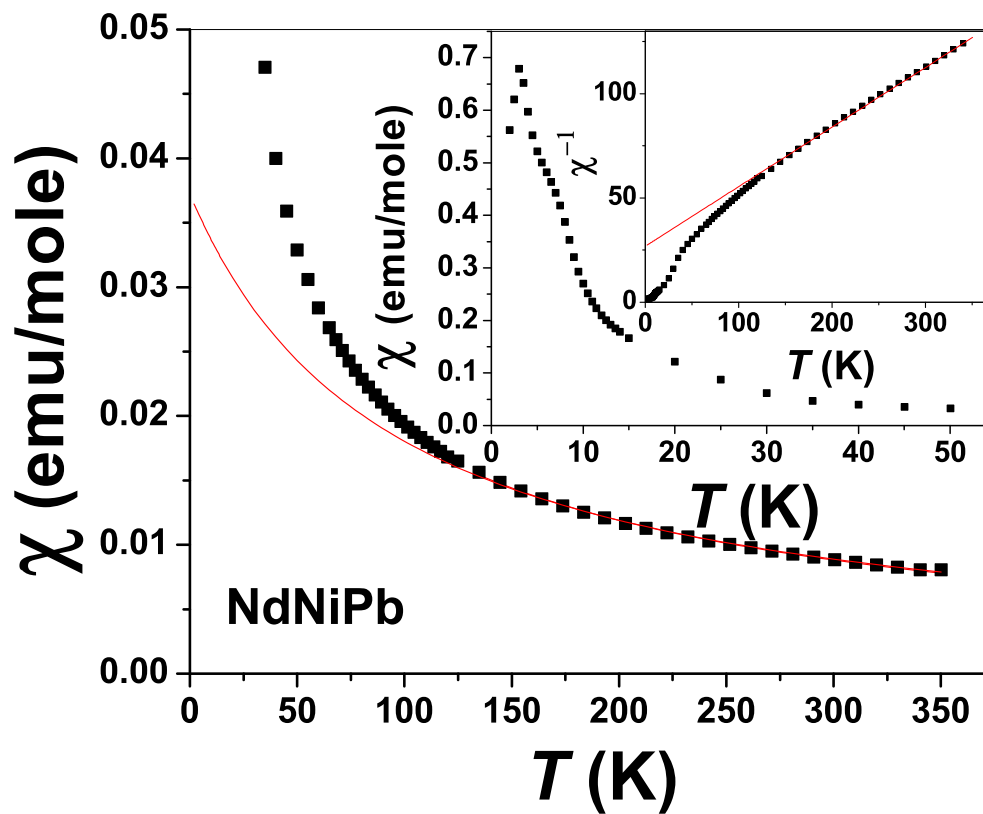
Fig. 17. Magnetization versus temperature for NdNiPb at 1000 Oe. The dashed curve shows a Curie fit from which p_{eff} is calculated. The inset figure shows the inverse susceptibility vs. temperature.

tion, I also obtained a consistent estimation of the CEF splitting energy for NdNiPb, and showed that the ground state is composed of a doublet. Resistivity measurements showed metallic behavior.

C.   NdCuGe

1.   Experimental

Samples of NdCuGe and LaCuGe were prepared for this study by arc melting the elemental constituents under argon atmosphere, using starting materials of 99.9 % purity. Ingots were re-melted several times. To ensure a homogeneous final material, samples were annealed at 800 °C for two months. The structure was analyzed by X-ray diffraction using Cu K_α radiation. Both samples were found to be single phase with the AlB_2 structure (space group designation $P6/mmm$, #191), with mixed occupation of Cu and Ge on B sites in the AlB_2 lattice, as reported elsewhere [15, 20]. Lattice constants from the X-ray fit for NdCuGe were found to be $a = 0.4277$ nm and $c = 0.3881$ nm, in good agreement with what has been reported in the literature.

A SQUID magnetometer was used to measure the DC magnetization in the temperature range 5–300K. The magnetic field was applied along the long axis of the sample in order to minimize the demagnetizing field. The temperature dependence of the heat capacity (C) was measured using an adiabatic method down to 2 K in the Quantum Design PPMS system.

2.   Results and Discussion

a.   Heat Capacity Measurements

Fig. 18 shows heat capacity results for both NdCuGe and LaCuGe for temperatures up to 250 K. At high temperatures both curves approach the classical value $3R \times N$, due
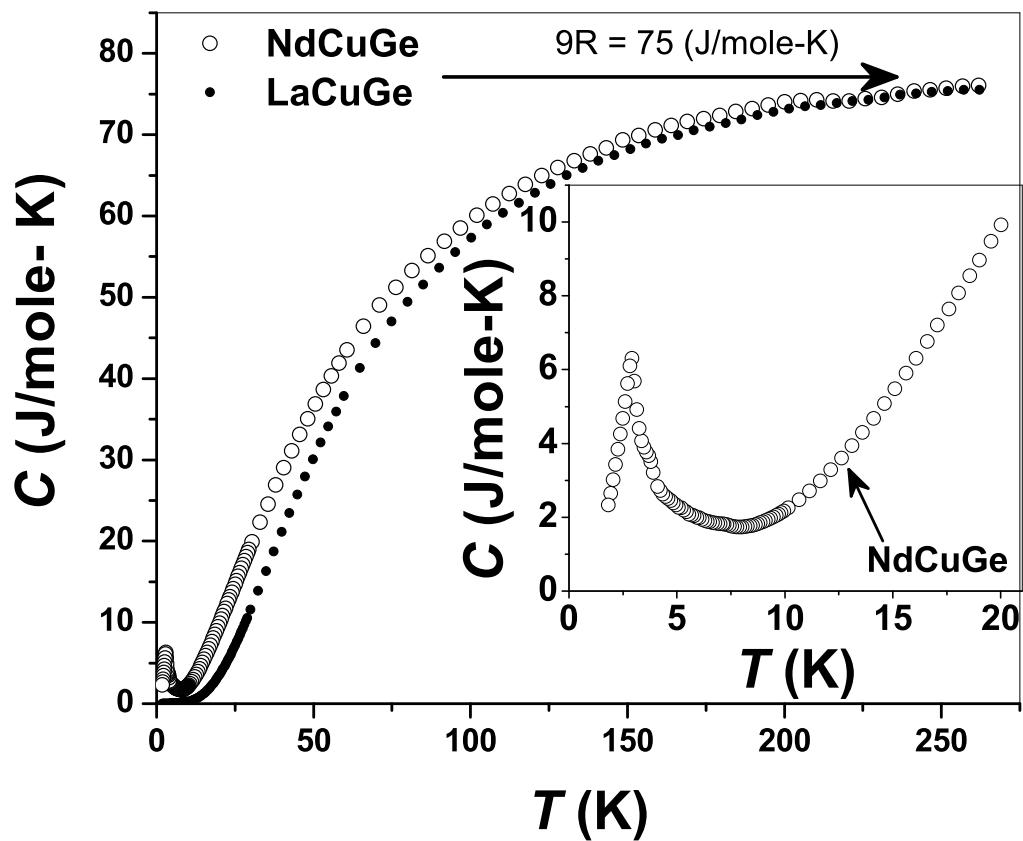
Fig. 18. Heat capacity for NdCuGe, and for nonmagnetic LaCuGe. Inset: low-temperature portion of NdCuGe data showing sharp feature at T_N (© American Institute of Physics).

to vibrational modes of the $N = 3$ atoms per formula unit, as seen in the figure. For the isomorphous nonmagnetic compound LaCuGe, the curve varies monotonically, with no anomaly observed down to 1.8 K. Below 10 K the LaCuGe heat capacity could be fitted to the equation $C = \gamma T + \beta T^3$, with electronic coefficient $\gamma = 2.22$ mJ/(mole K^2), and β corresponding to a Debye temperature (Θ_D) equal to 231 K in the low-T limit. After subtracting the electronic contribution, γT, we also fit the full temperature dependence to a Debye model according to established procedure [24]. In this fit the effective Θ_D rises to a low-temperature peak of 280 K near T = 10 K, followed by a minimum of $\Theta_D = 240$ K near 30 K and a broad maximum of $\Theta_D \approx 260$ K near 100 K, which is shown in Fig. 19. This variation in Debye temperature could be due to the deviation of phonon density of states $D(\omega)$ from ω^2 (Eqn. 2.2). In the NdCuGe heat capacity, the step-like feature centered about approximately 3.1 K (inset of Fig. 18) corresponds to the antiferromagnetic transition previously identified [20], while the difference between the NdCuGe and LaCuGe curves at higher temperatures can be attributed to the effect of crystalline electric field (CEF) splitting of the Nd magnetic levels.

I isolated the magnetic contribution to the heat capacity (ΔC_{mag}) by subtracting an interpolated LaCuGe curve from that of NdCuGe. In doing so, temperatures for LaCuGe were scaled proportional to $\sqrt{M_{LaCuGe}/M_{NdCuGe}}$, where the terms in the ratio are molar masses. (A method utilizing partial Debye temperatures [38] gives nearly identical results, as does simply using data uncorrected for the masses.) The resulting ΔC_{mag} is shown in Fig. 20. Above the low-temperature magnetic transition region a Schottky-like anomaly is seen, due to the freezing out of CEF-split magnetic levels. From (ΔC_{mag}) we obtained the magnetic entropy using the relation $S_{mag} = \int (\Delta C_{mag}/T)dT$, with the result shown in the inset of Fig. 20. A power-law extrapolation below 1.8 K shows that approximately 0.1 R should be added to
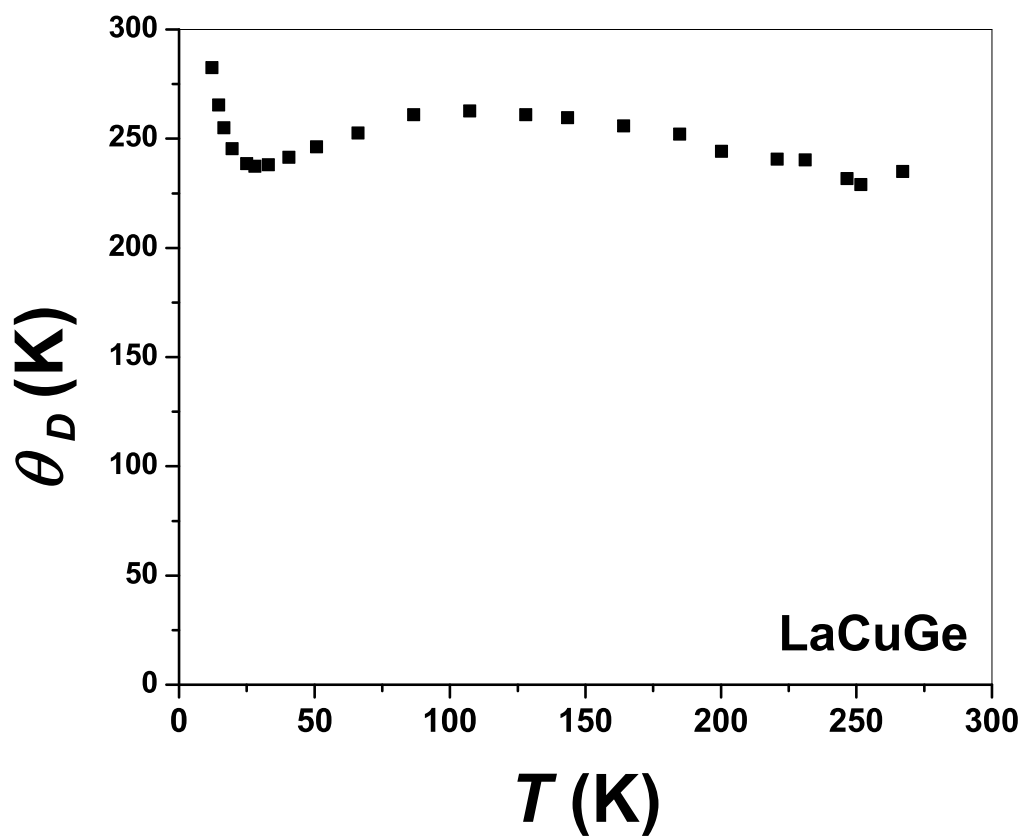
Fig. 19. Debye temperature for LaCuGe as a function of temperature showing a sharp peak, a minimum and a broad maximum.

the entropy due to the heat capacity at these temperatures below the measurement range. This small correction has not been included in the inset figure. S_{mag} reaches a plateau at high temperatures, very close to the expected total magnetic entropy $S/R = \ln(2J + 1) = 2.30$ for $J = 9/2$ per Nd. This is shown by the horizontal arrow in the inset figure. This result is consistent with the expected $J = 9/2$ state for trivalent Nd, and it provides additional confidence in the subtraction of the lattice and electronic parts of C. As can be seen from the inset, S_{mag} has its largest drop over the temperature range corresponding to the Schottky-like peak in ΔC_{mag} due to CEF splitting, while a further drop is observed near T_N.

Nd levels within the point-group symmetry of NdCuGe, including atomic disorder on the Ge and Cu sites, may be split into 5 separate Kramers doublets [37], so I used a theoretical expression similar to what was used for NdNiPb, allowing the energies of the 5 doublets to vary arbitrarily in a least-squares fit to $\Delta C_{mag}(T)$ above 17 K. This relationship provided an excellent fit to the data, as shown in the solid curve in the main plot of Fig. 20. The fitting result, with levels shown schematically in Fig. 20, corresponds to a doubly degenerate ground-state with quadruplets at energies of 65 K and 146 K relative to the ground state. Thus, despite the Ge and Cu site-disorder, the fitted level multiplicity is the same as for the six-fold axial symmetry of the hexagonal virtual lattice, for which two quadruplets and one doublet would be expected [37].

The drop in entropy near T_N shown in Fig. 20 is close to that expected for a two-level ground state, although the theoretical value $\Delta S/R = \ln(2) = 0.69$ is not reached until a temperature of 9.1 K, corresponding to the extent of the visible tail in Fig. 20. Similarly, the jump in ΔC_{mag} at T_N is much smaller than the value $1.5R$ expected for a two-level ground state [23]. Although fluctuations will normally reduce this value, the present result is considerably smaller than observed, for example, in Nd_2Ni_2Pb [12] or a series of commensurate-antiferromagnetic Gd compounds [38].
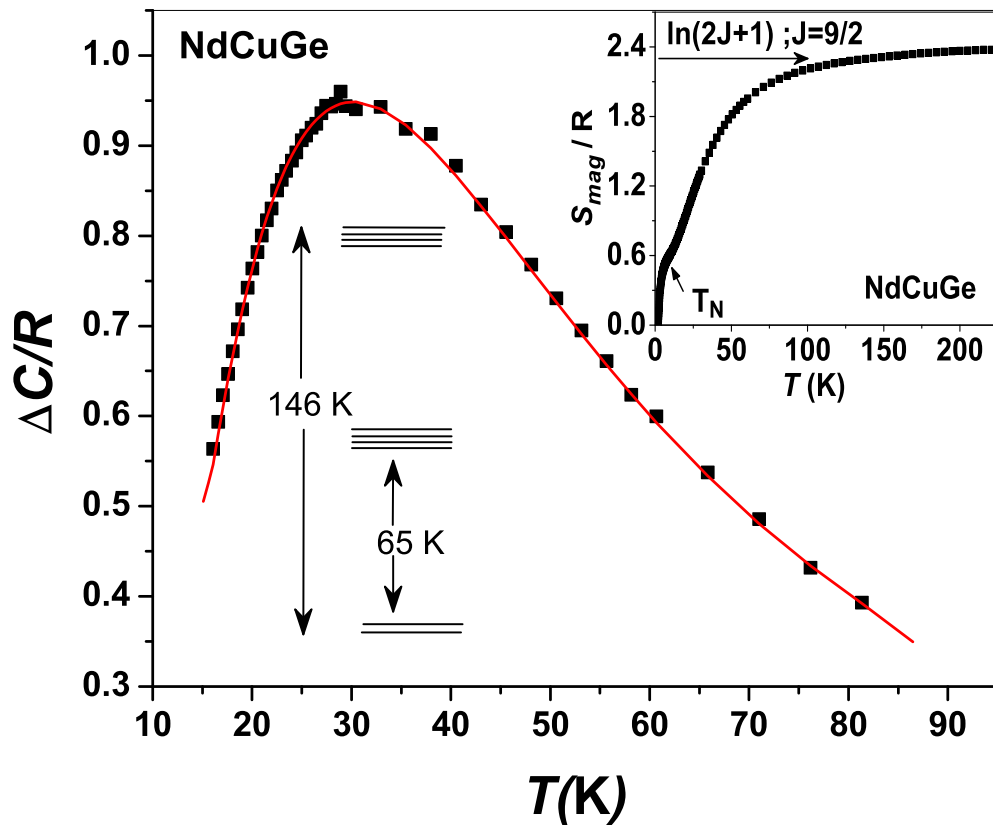
Fig. 20. Magnetic contribution to the heat capacity of NdCuGe at zero field, normalized to the ideal gas constant. Solid curve shows Schottky-anomaly fit for crystal-field-split levels as described in the text. Splitting of these levels is shown schematically below the data. Inset: Magnetic entropy extracted from the heat capacity.

The enhanced fluctuations may be due to the atomic-site disorder on the AlB_2 lattice in the present case.

b. Magnetic Measurements

Measurements of magnetization (M) vs. temperature show the expected peak above 3 K corresponding to the antiferromagnetic transition. In Fig. 21 the data are plotted as $(1/M)$ to show the Curie-Weiss behavior. In light of the CEF splittings obtained from the heat capacity, paramagnetic behavior for $J = 9/2$ local moments should be observed well above the temperature corresponding to the largest splitting energy (146 K). Such a fit above 240 K yields a negative Curie temperature $\theta_N = -12$ K, and an effective moment $p_{eff} = 3.62$. The latter is identical to the free-ion moment for Nd, showing that the magnetic moment resides in Nd local moments. Note that by extending the fitting range down to 80 K, we obtained a somewhat reduced value, $\theta_N = -7.5$ K, identical to the previously reported result [20], however it is now clear that CEF splitting of Nd levels comes into play for this temperature range.

Below 10 K, $1/M$ drops off due to the nearness of the magnetic transition. However, for a narrow range of 14–25 K, Curie-Weiss behavior is also observed, with a least-squares fit yielding $p_{eff} = 3.16$, and a small positive paramagnetic Curie temperature. The small positive Curie temperature associated with an antiferromagnetic transition seems at first surprising, however it is similar to the result [20] for PrCuGe, and could result from competing interactions in different crystallographic directions. Neutron scattering already showed a magnetic structure consistent with antiferromagnetic coupling between inter-plane moments and ferromagnetic coupling between intra-plane moments [20]. The fitted curve is shown by a second straight line in the figure. For a ground-state CEF doublet composed of levels $\pm m_J$, p_{eff} will be $2gm_J\sqrt{3/4}$. Taking $g = 8/11$, which is the Landé g-factor for $J = 9/2$ Nd, the
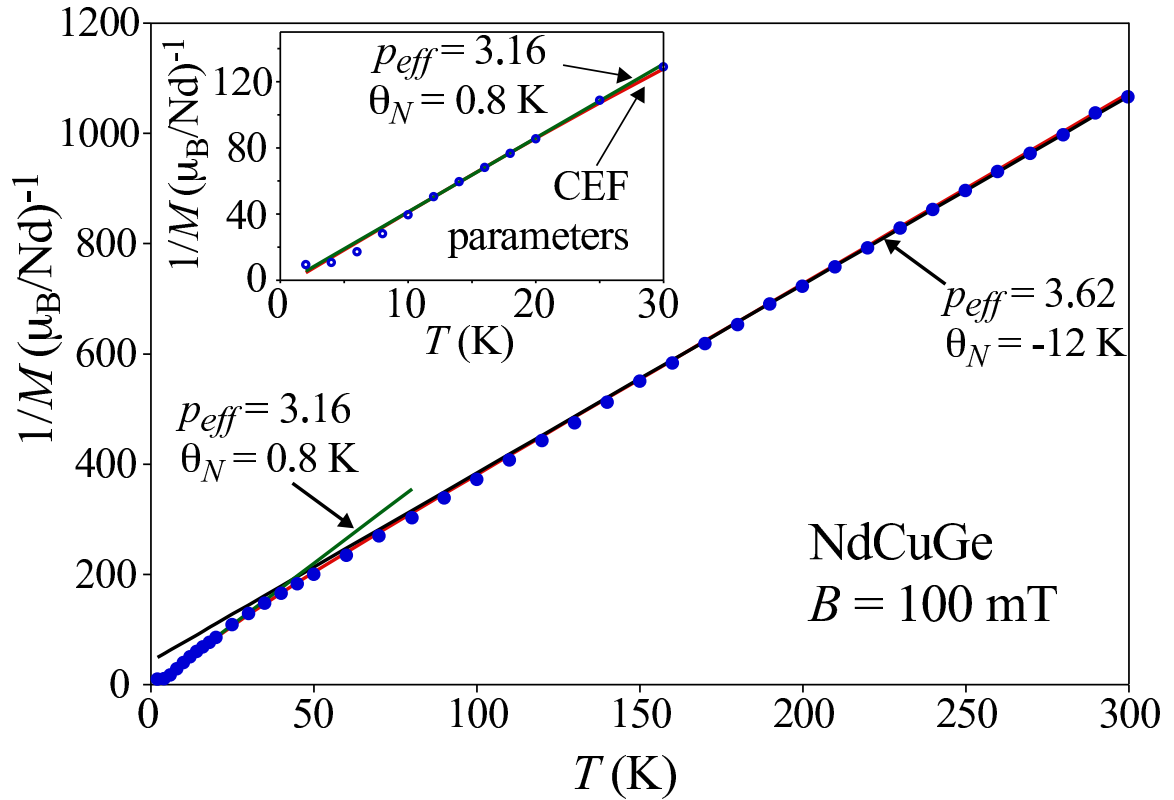
Fig. 21. Inverse magnetization for NdCuGe measured in a DC field of 100 mT. Straight lines: Curie-Weiss fits with effective moments 3.16 μ_B at low temperatures and 3.62 μ_B at high temperatures, as labeled. Solid curve: calculated result obtained using crystal electric field (CEF)-split levels with model described in text. Inset: expanded view at low temperature, with high-temperature Curie-Weiss fit omitted for clarity. (© American Institute of Physics).

observed $p_{eff} = 3.16$ yields $m_J = 2.51$, indicating that the ground-state doublet is likely composed of pure $\pm 5/2$ levels, with $m_J \equiv 2.5$. With this as a basis, I found very satisfactory agreement above the magnetic transition, using CEF values from the heat capacity with no additional parameters, by assuming that the ground state doublet is composed of $\pm 5/2$ levels, and that the 65 K levels are $\pm 3/2$ and $\pm 7/2$ and the 146 K levels $\pm 1/2$ and $\pm 9/2$. The magnetization resulting from this model is shown by the solid curve in Fig. 21, which nearly coincides with the straight-line fits except in the cross-over region, as indicated in the inset. Note that for the CEF-based curve, no magnetic interactions (hence no θ_N) were included.

Additional information is provided by M vs. H curves, shown in Figs. 22 and 23. At 15 K (Fig. 22), a Brillouin function corresponding to a doublet of $\pm 5/2$ levels (solid curve) follows the data quite closely. For this temperature and range of fields, occupation of the CEF-split levels is negligible, so that the magnetic state at low temperatures can be regarded accurately as being built from the $\pm 5/2$ ground-state levels only. At 2 K, saturation is incomplete in a field of 7 T (Fig. 23), however a fitted extrapolation function of the form [29] $M = A/H + B/H^2$ yielded a saturation moment of 1.88 μ_B. This is nearly identical to the value corresponding to $gm_J = (8/11)(5/2) = 1.82$ expected for a magnetic state composed of $\pm 5/2$ levels. This saturation moment is somewhat larger than the value (1.24) previously deduced from neutron scattering [20] at 1.6 K, the difference likely resulting from a combination of thermal agitation in the neutron measurement and local variations in moment orientation due to site disorder in NdCuGe. The difference comes about since the scattering measurement determines the average spontaneous moment where as the saturation result determines the forced alignment limit.
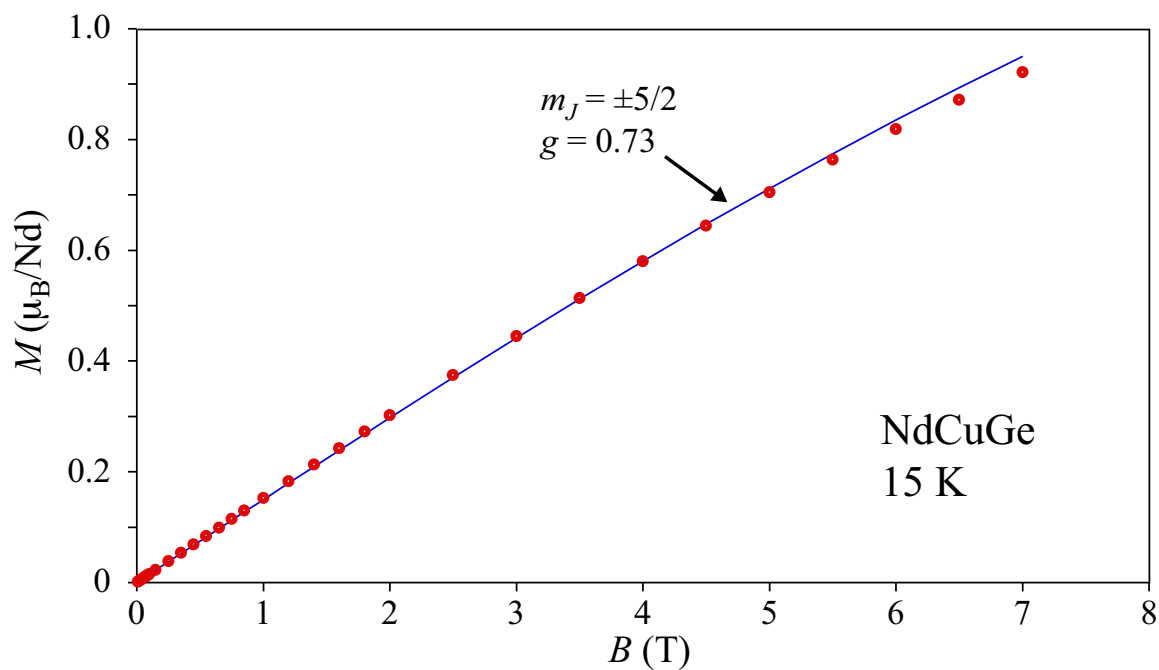
Fig. 22. Magnetization vs. field up to 7 T for NdCuGe at 15K. Solid curve: Brillouin-function fit, for g and J_z as labeled. (© American Institute of Physics).
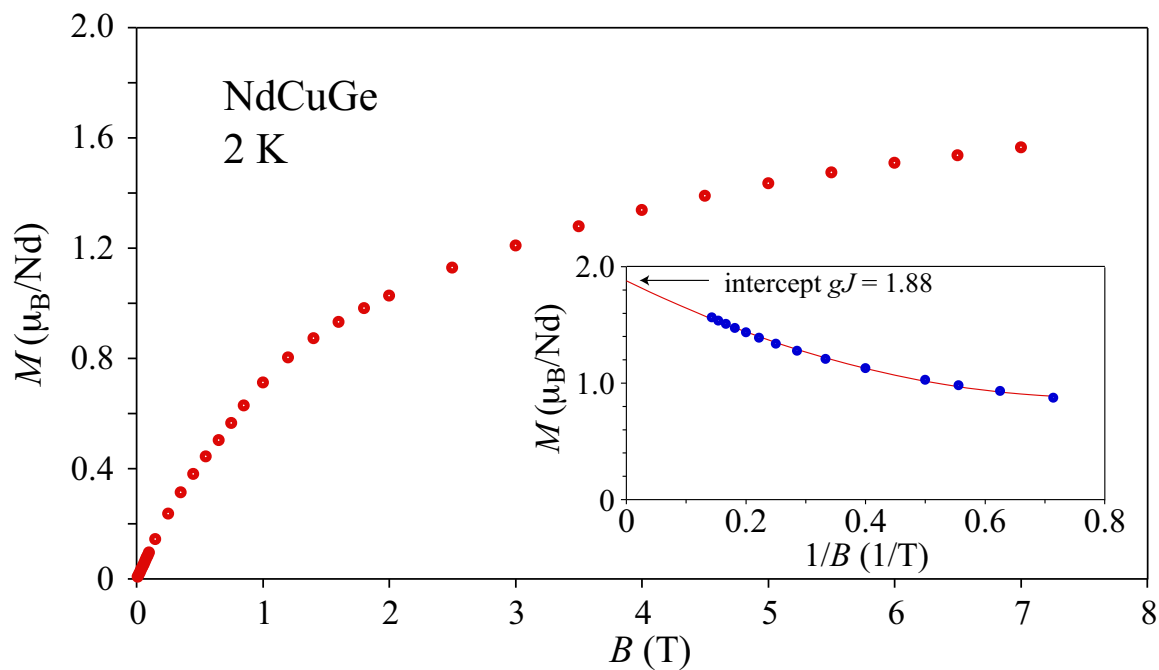

Fig. 23. Magnetization vs. field up to 7 T for NdCuGe at 2K. Inset: fit yielding saturation moment. (© American Institute of Physics).

3. Resistivity Measurements

The resistivity for this sample was measured by Y. Oner. I have including our published results [19] for comparison. Oner fit the measurements to a model involving CEF-split levels. The best-fit values, $\Delta_1 = 65$ K, $\Delta_2 = 159$ K, are shown in Fig. 24. A very good fit was obtained over the entire temperature range where magnetic scattering dominates, and the CEF splittings obtained are in good agreement with the heat capacity analysis. This is the same level scheme that also provided good agreement for the temperature dependence of the dc susceptibility.

4. Conclusions

We have carried out magnetization, magnetic susceptibility and electrical resistivity measurements on NdCuGe. The magnetization is dominated by Nd^{3+} ionic moments at high temperatures, while at low temperatures CEF splitting of the rare-earth levels comes into play. With the combination of measurements we obtained a consistent estimation of the CEF splitting energies, and showed that the ground state is composed of a $J_z = 5/2$ doublet. Saturation measurements showed that the previously-observed low-temperature magnetic state is formed from this doublet. The resistivity fit results are in good agreement with heat capacity and magnetization.

D. Other Related Materials

1. CeCuGe Results

CeCuGe is an interesting system because spin fluctuation behavior and an anomalous exponent for thermopower near the ferromagnetic transition has been observed in recent work in our laboratory [17]. In previous work, magnetization measurements yielded a ferromagnetic $T_c = 10$ K and a Curie fit for temperatures greater than 20
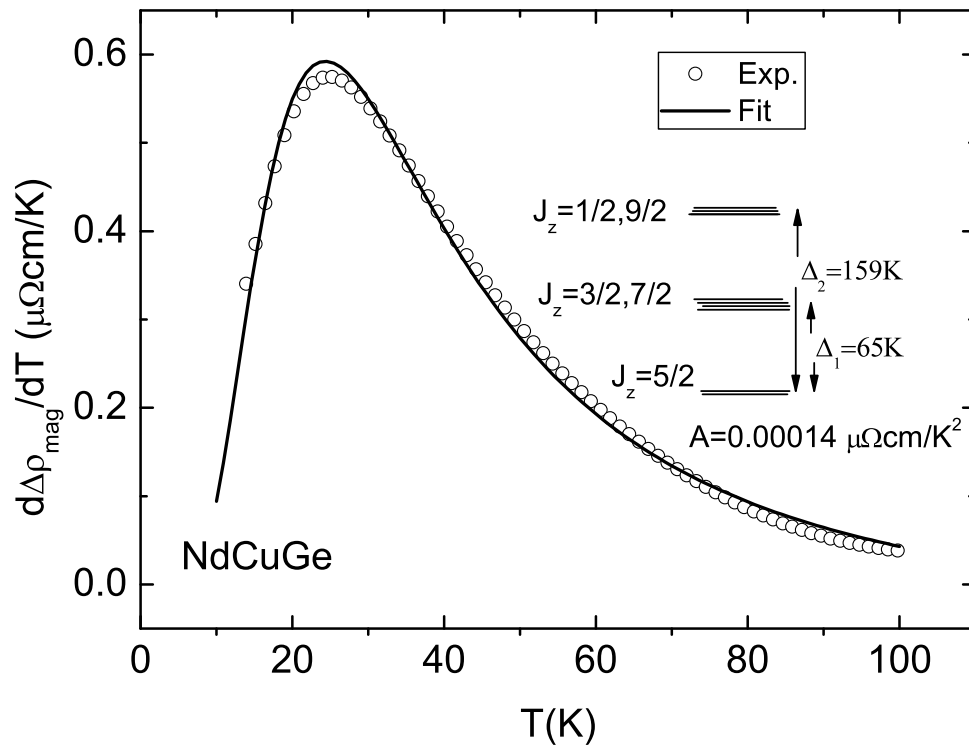
Fig. 24. Temperature derivative of electrical resistivity (ρ_{mag}, with Bloch-Grüneisen fit subtracted), plotted vs. T, and theoretical curve based on CEF model in reference. Fitted CEF parameters are also illustrated, along with fitted T^2 coefficient, A. This result is included to illustrate consistency with specific heat measurements described in this work. (© American Institute of Physics)

Fig. 25. Field dependent heat capacity of CeCuGe showing gradual broadening of 10
K transition, which disappears at high field.

K yielded an effective moment very close to the expected Ce^{3+} free ion moment [17]. In new work, M vs H measurements at 2 K and 15 K show a clear difference due to the ferromagnetic transition. Heat capacity measurements display a sharp peak at T_c, with peak position shifting towords higher tempera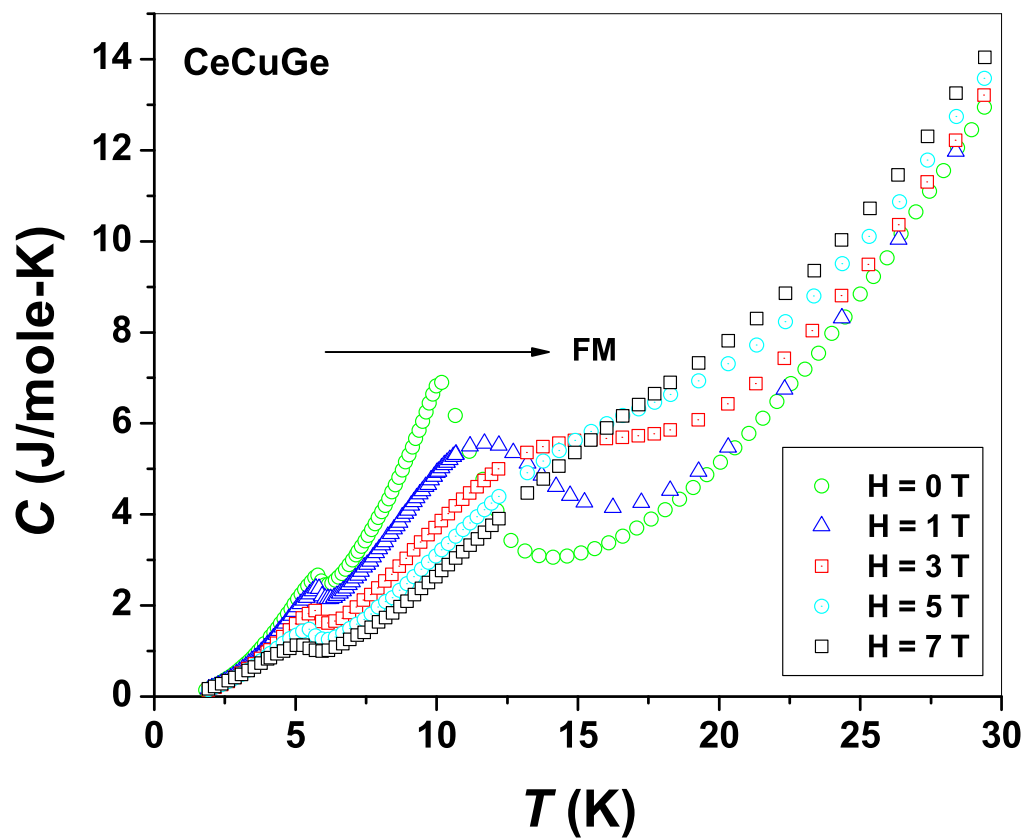tures as the applied magnetic field increases. Field dependent heat capacity is shown in Fig. 25. In larger fields the peak moves to higher temperatures, signaling that the transition is of ferromagnetic character. The peak disappears above 7 T. NMR results show that the Knight shift is positive and the line width becomes very broad as we go to low T. The line broadening is due to dominant ferromagnetic fluctuations.

2. GdCuGe Results

Magnetization and heat capacity data for GdCuGe are shown in Fig. 26. GdCuGe undergoes a single antiferromagnetic transition at T_N= 17 K, the highest transition temperature for this series, T_N is consistent with previously reported results [16]. Magnetization vs. temperature measurements at 1000 Oe show a sharp peak at the transition temperature. Heat capacity results also confirm the transition, while field dependent heat capacity shows that the peak shifts towards lower temperatures. Interestingly all curves cross at same point; similar behavior has been observed in other correlated systems [39]. Resistivity measurements also show a kink at T_N, while at high temperature metallic behavior is seen. To better understand the magnetism of these materials I did some local probe NMR measurements. Results of the line shape, and Knight shift measurements, show that the coupling mechanism is dominated by the exchange interaction.
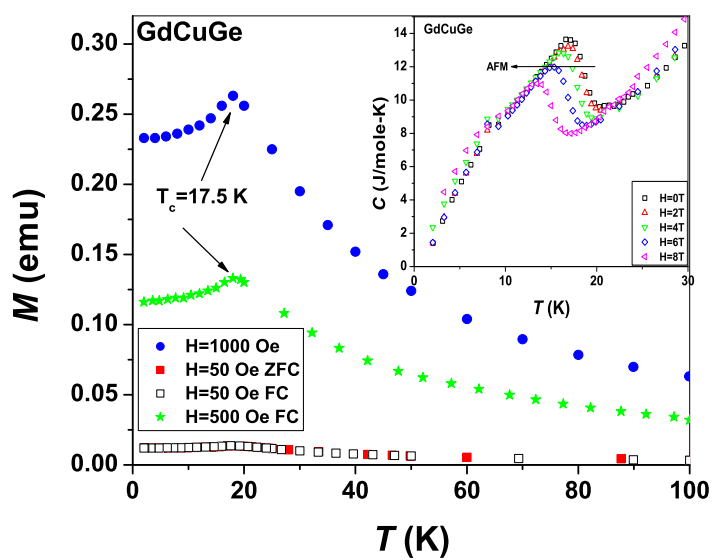
Fig. 26. Heat capacity for GdCuGe, and for nonmagnetic LaCuGe. Inset: low-temperature portion of GdCuGe data showing a sharp feature at T_N and its change with field.

E. $R_5\mathrm{NiPb}_3$

1.   Experimental

Polycrystalline samples of $R_5\mathrm{NiPb}_3$ ($R=$ La, Ce, Nd, Gd) were prepared by melting the elements with purity of 99.99 % in an arc furnace with a water-cooled copper hearth under argon atmosphere. Ingots were re-melted several times to insure homogeneity and annealed at 670 K for Ce, 870 K for Nd and Gd, for four weeks. The structure was analyzed by X-ray diffraction using Cu K_α radiation. All materials were found to have the hexagonal $\mathrm{Hf}_5\mathrm{CuSn}_3$ structure (space group #193: $P6_3/mcm$). Crystal structure parameters for all samples are consistent with reported values [8, 9].

DC magnetization was measured between 2 and 350 K with the field up to 7 T along the long axis of the sample to minimize the demagnetizing field. The heat capacity was measured between 2 and 300 K.

2.   Results and Discussion

I found that $\mathrm{Ce}_5\mathrm{NiPb}_3$ exhibits a ferromagnetic transition at $T_c = 48$ K, $\mathrm{Gd}_5\mathrm{NiPb}_3$ at $T_c = 68$ K; whereas, $\mathrm{Nd}_5\mathrm{NiPb}_3$ exhibits an antiferromagnetic phase transition at 42 K. Transport properties showed all three to exhibit metallic behavior.

a. $\mathrm{La}_5\mathrm{NiPb}_3$

I measured heat capacity of $\mathrm{La}_5\mathrm{NiPb}_3$ as a non-magnetic comparison for temperatures up to 250 K, and magnetic fields of 0 and 1 T. Results are shown in Fig. 27. At high temperatures both curves approach the classical value $3R \times N$, due to vibrational modes of the $N = 9$ atoms per formula unit, as seen in the figure. The curves vary monotonically, with no anomaly observed down to 1.8 K even in the 1 T magnetic
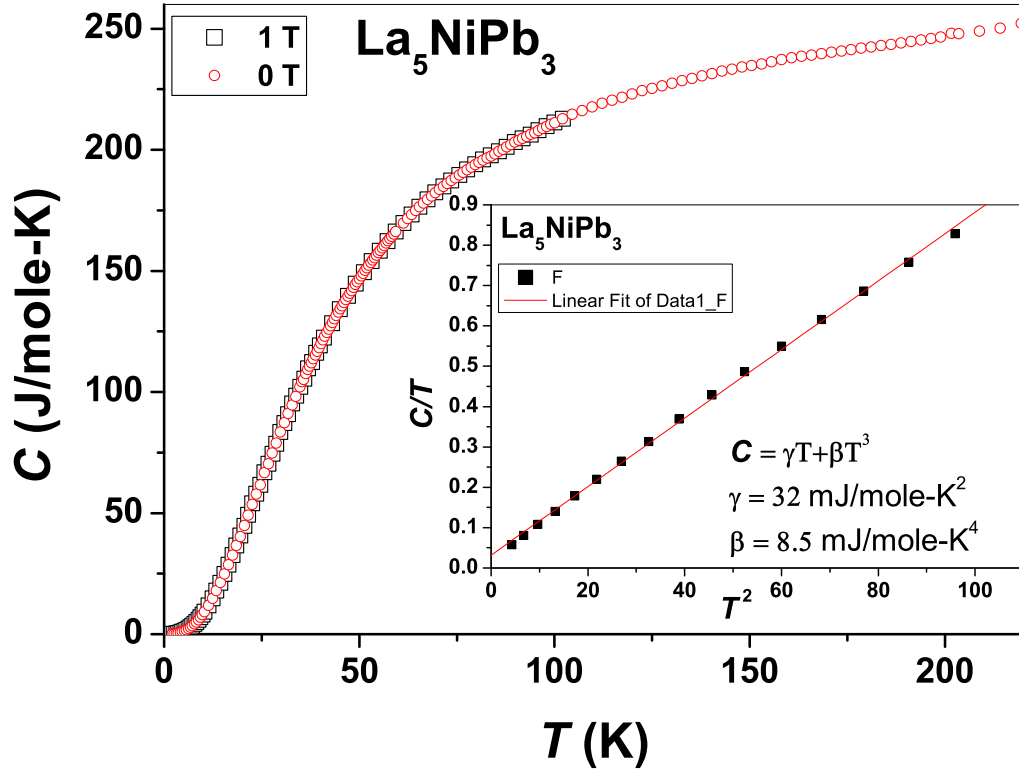
Fig. 27. Heat capacity versus temperature for La_5NiPb_3. In the inset, C/T data at $H = 0$ T are plotted as a function of T^2 along with a linear fit.

field, which confirms that Ni is nonmagnetic. Below 10 K the La_5NiPb_3 heat capacity could be fitted to the equation $C = \gamma T + \beta T^3$, with electronic coefficient $\gamma = 32$ mJ/(mole K^2), and $\beta = 8.5$ mJ/(mole K^4).

b. Ce_5NiPb_3

Fig. 28 shows heat capacity results for Ce_5NiPb_3. The high temperature heat capacity approaches the classical value $3R \times N$ similar to La_5NiPb_3.

The Ce_5NiPb_3 heat capacity shows a distinct step-like peak at 48 K (Fig. 28), characteristic of long range magnetic order. At high fields the peak moves to higher
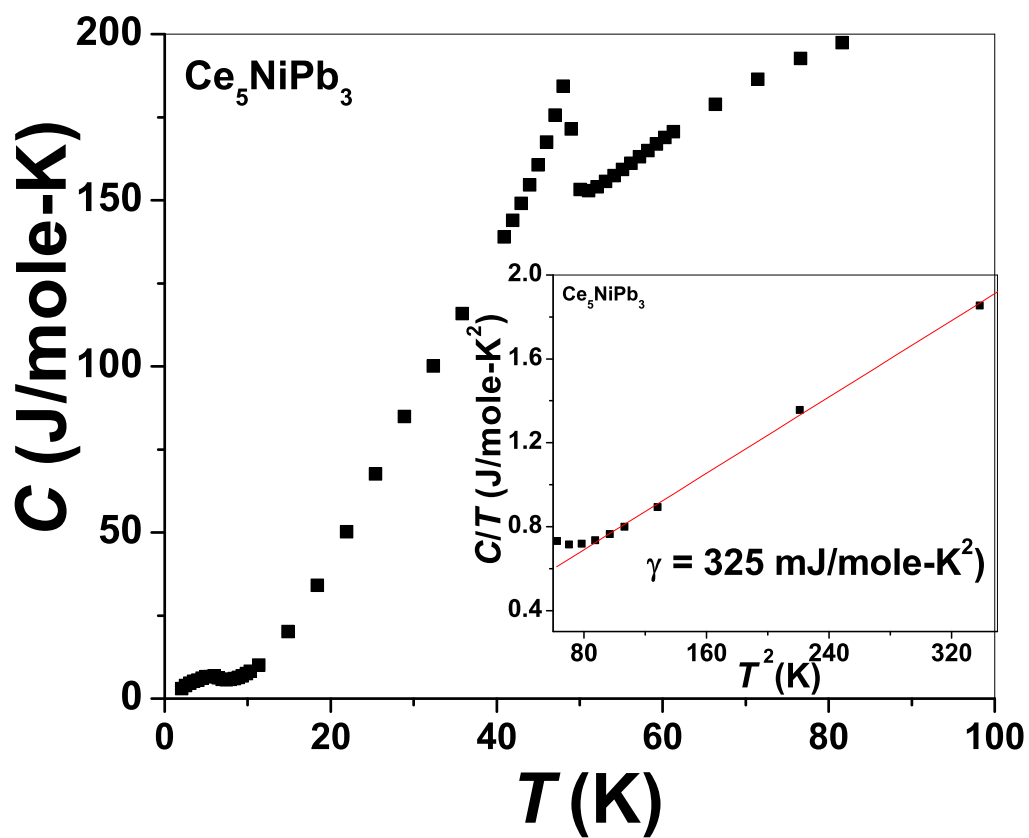
Fig. 28. Specific heat for Ce_5NiPb_3 showing step like transition at 48 K. Inset: Low temperature specific heat with linear fit.

temperatures, signaling that the transition is of ferromagnetic character. The low temperature specific heat fits to $C = \gamma T + \beta T^3$, with a large γ of 325 mJ/mol-K^2. This could be due to heavy Fermion behavior.

I isolated the magnetic contribution to the heat capacity (ΔC) by subtracting an interpolated La$_5$NiPb$_3$ curve from that of Ce$_5$NiPb$_3$. The resulting ΔC is shown in the inset of Fig. 29; two transitions are seen. From (ΔC) I also obtained the magnetic entropy using the relation $S_{mag} = \int (\Delta C / T) dT$, with the result shown in Fig. 29. S_{mag} reaches two plateaus near two transition temperatures, but the corresponding values are less than the total magnetic entropy $S = 5\text{Rln}(2J + 1)$ with $J = 1/2$ for the first transition, and with $J = 5/2$ for the second transition. This lack of entropy saturation could be due to CEF excited states far from the ground states. However, lack of complete ordering is another possibility, as discussed later. The peak seen at low T I attribute to a known [40] oxide phase. Note that Ce compounds are relatively more sensitive to air and have oxidation problems; this could be the reason why S has a down-turn instead of a plateau near 10 K.

I also measured the magnetization as a function of magnetic field and temperature, and found that the results agree with the Curie-Weiss law at high temperatures indicating a paramagnetic state. Zero Field Cooled (ZFC) and Field Cooled (FC) magnetization of Ce$_5$NiPb$_3$ are shown in Fig. 30. The ZFC snd FC curves diverge at 48 K, an irreversibility temperature which coincides with the peak seen in heat capacity measurements. A high T, above 100 K, the Curie fit yields an effective moment, $\text{p}_{eff} = 2.43$, very close to the expected Ce^{3+} value of 2.54 for $J = 5/2$ (according to Hunds rule) [6] indicating that the 3d electrons of Ni have no localized moments. The fit has $\theta_p = 8$ K indicating a ferromagnetic tendency, and the peak at 48 K is consistent with the specific heat anomaly at the same temperature. As T is lowered, there is a gradual deviation from the Curie-Weiss law. Since this compound forms
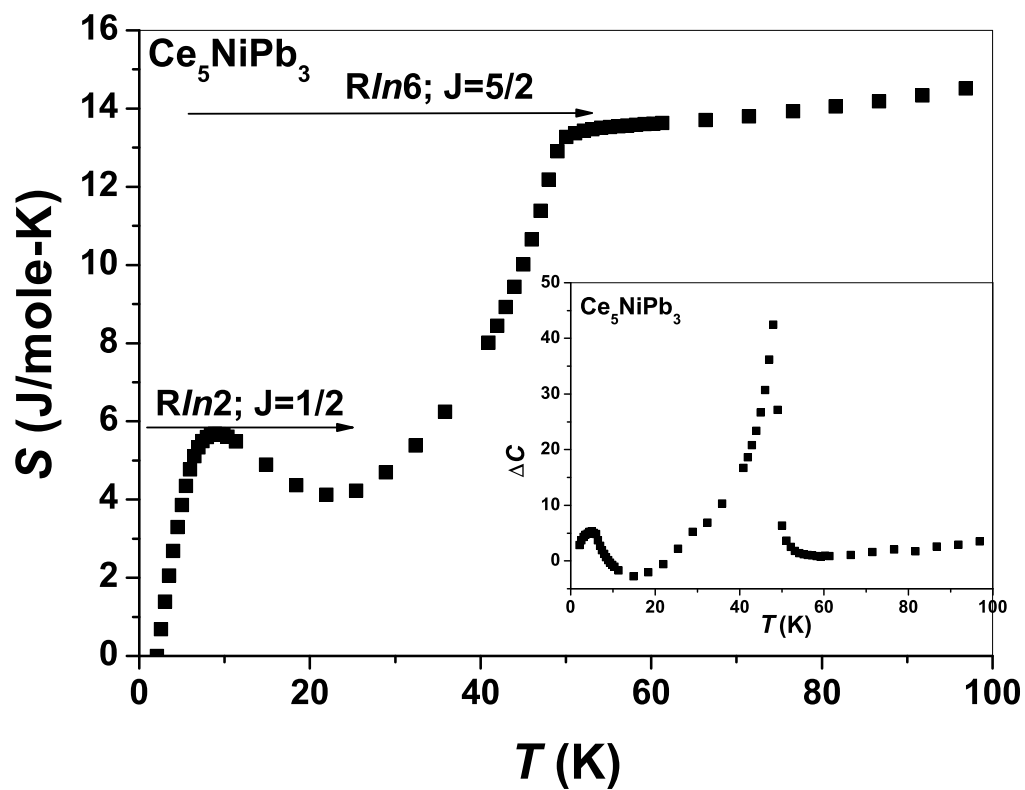
Fig. 29. Magnetic entropy as a function of temperature from specific heat difference described in text. In the inset, plot of magnetic heat capacity versus temperature for Ce_5NiPb_3 showing the peak at 48 K.
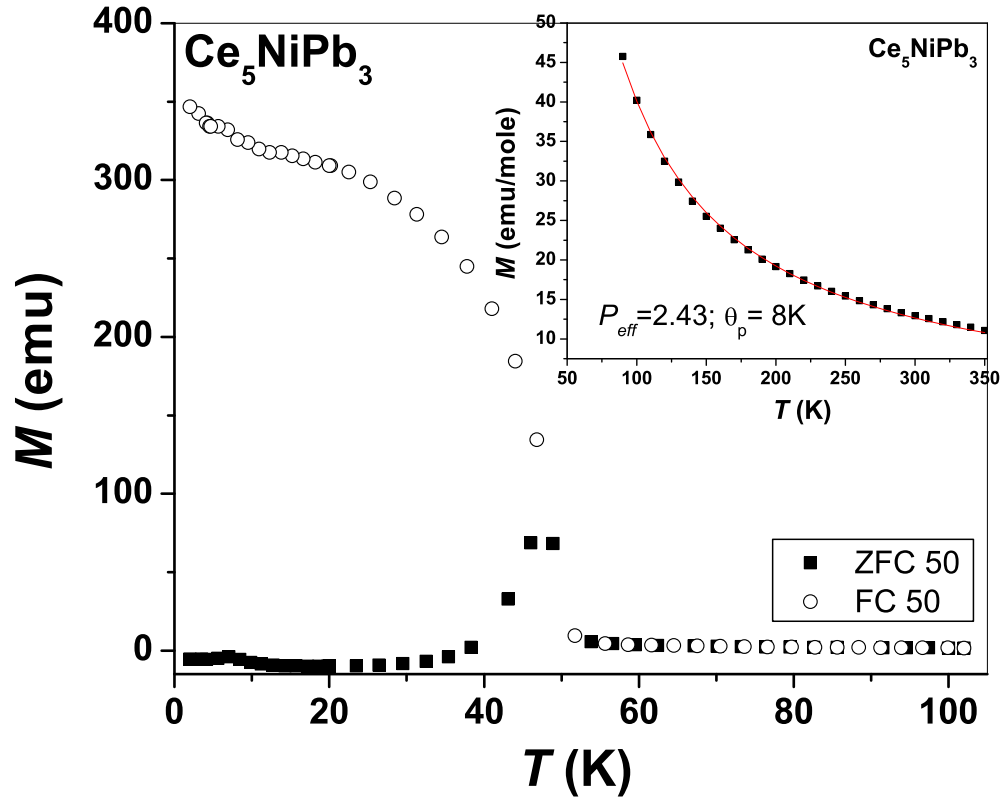
Fig. 30. ZFC, FC magnetization versus temperature for Ce_5NiPb_3 at field=50 Oe . The dashed curve in the inset shows a Curie fit from which we calculated p_{eff} and θ_p.

in a hexagonal structure, it is expected that the crystal-field-split ground state is a doublet [37]. It should be noted that the value of θ_p obtained from the high temperature data (see the inset of Fig. 30) has a positive sign, and, therefore, the exchange interaction corresponding to the doublet ground state is ferromagnetic. This is also consistent with heat capacity data.

$M - H$ measurements at 1.8 K show lack of saturation, thus the transition is presumably ferrimagnetic. As seen in Fig. 31 the value of the highest magnetic mo-

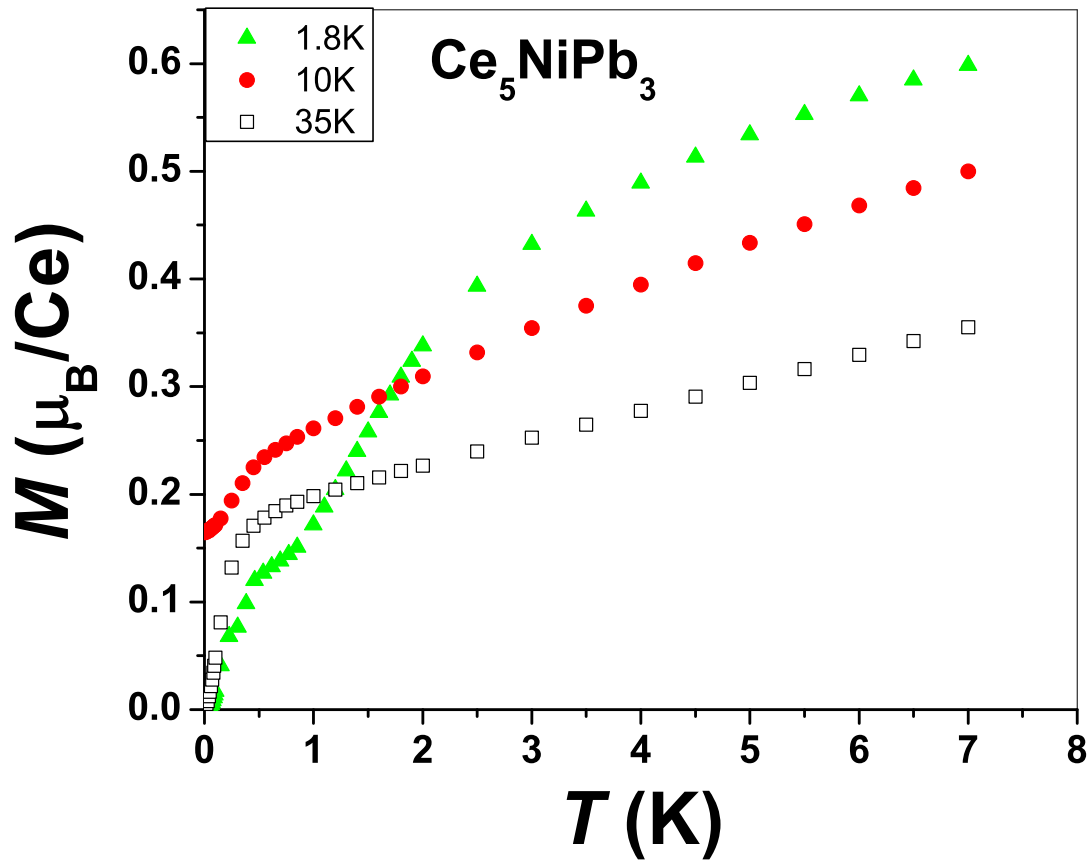Fig. 31. Magnetization vs. field for Ce$_5$NiPb$_3$ at different temperatures.

ment reached is less than 0.7 μ_B even at very high fields. The 1.8 K curve also shows a metamagnetic transition at approximately 0.4 T.

c.   Nd$_5$NiPb$_3$

The Nd$_5$NiPb$_3$ heat capacity has a peak at 42 K, and a small feature at 8 K, as seen in Fig. 32. The low-temperature specific heat could be fitted to the equation
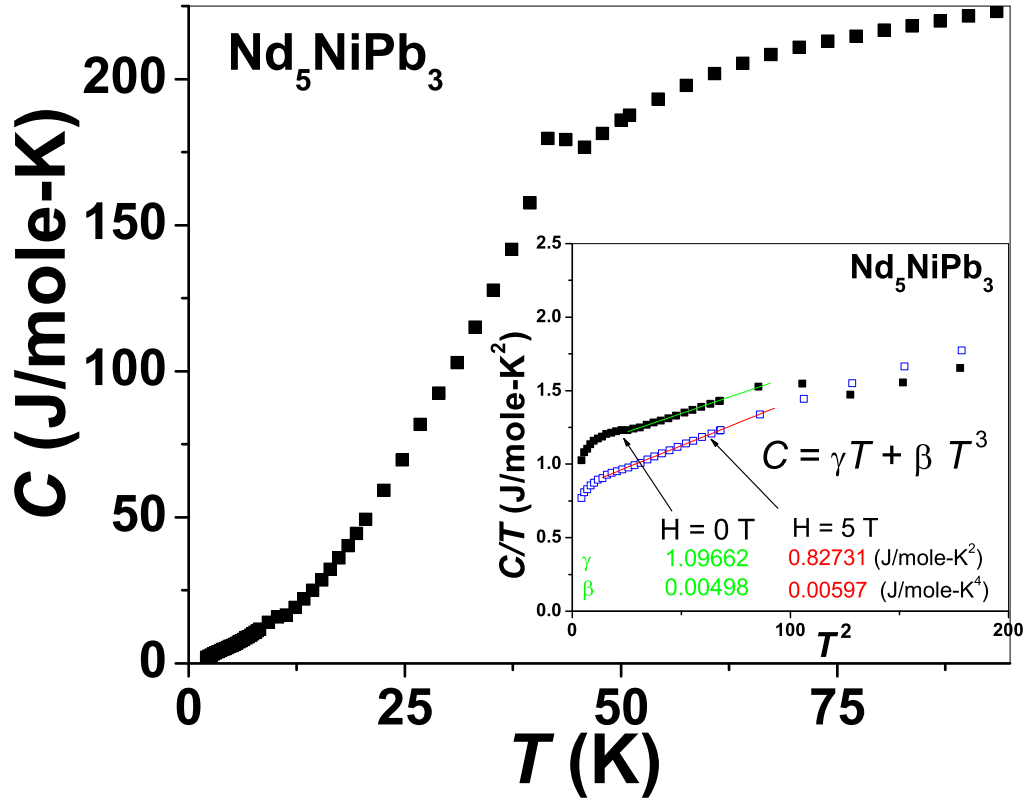
Fig. 32. Heat capacity versus temperature for Nd_5NiPb_3 shows a peak at 42 K . In the inset, C/T data are plotted as a function of T^2 and its linear fit is shown for $H=$ 0 T and 5 T.

$C = \gamma T + \beta T^3$ over the temperature range 5 K to 10 K, with zero-field electronic coefficient $\gamma = 1.096$ J/(mole K^2), and $\beta = 4.98$ mJ/(mole K^4), as seen in the inset of Fig. 32. This value of γ is higher than expected for Nd based intermetallics, and likely results from spin fluctuations related to the low-temperature transition.

I isolated the magnetic contribution to the heat capacity (ΔC) by subtracting an interpolated La_5NiPb_3 curve from that of Nd_5NiPb_3. The resulting ΔC is shown in inset of Fig. 33; in this case it appears that 42 K magnetic transition interrupts the CEF Schottky-like anomaly. From (ΔC) we obtained the magnetic entropy using
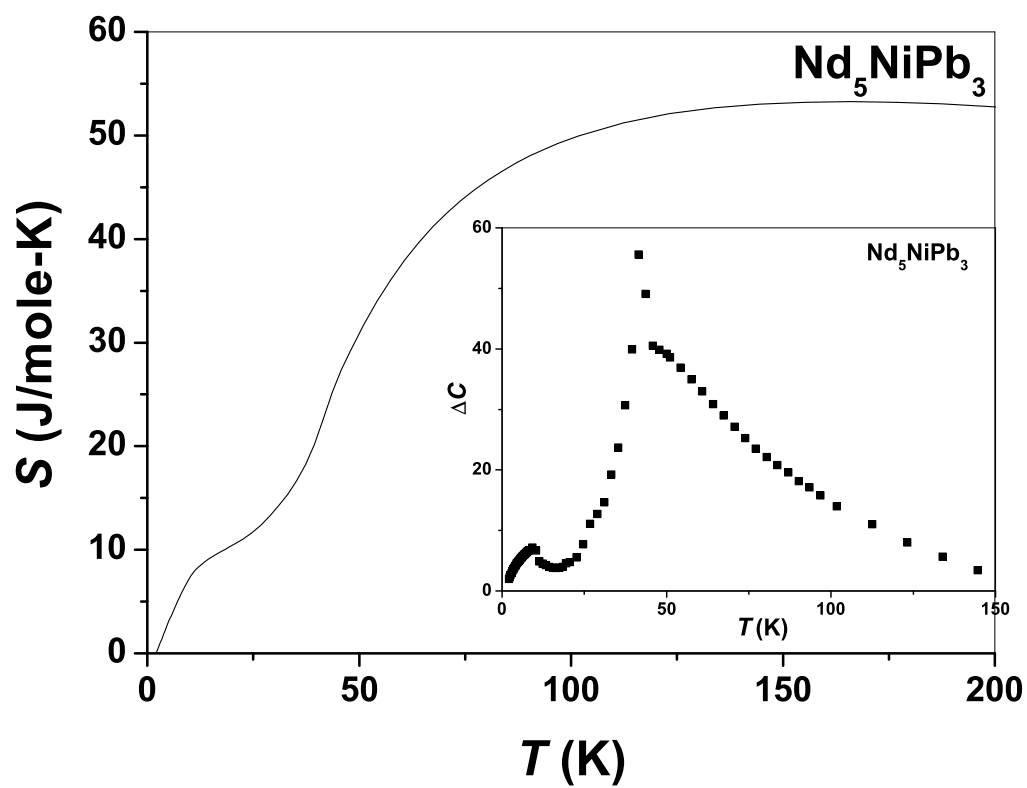
Fig. 33. Nd_5NiPb_3 magnetic entropy as a function of temperature. In the inset, a plot of magnetic heat capacity versus temperature for Nd_5NiPb_3 showing a peak at 42 K.
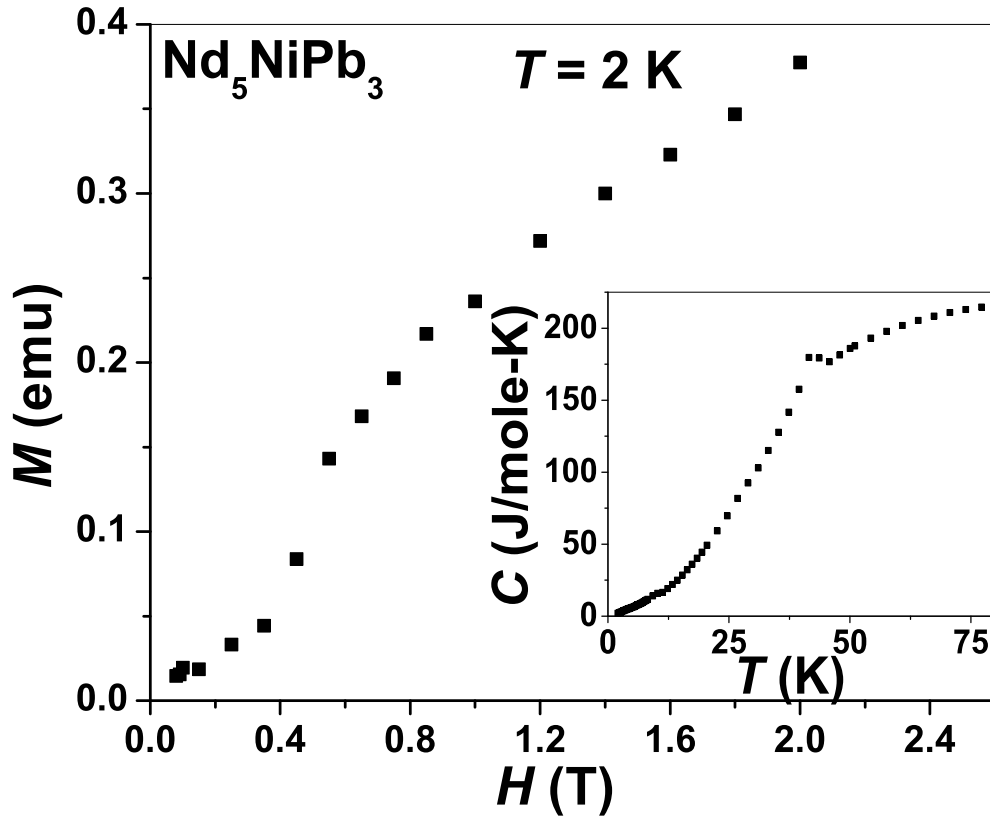
Fig. 34. Magnetization vs. field for Nd_5NiPb_3 at 2 K showing metamagnetic behavior. Inset shows heat capacity vs. temperature.

$S = \int (\Delta C/T) dT$. The resulting S reaches a plateau at high temperatures, which is less than the total expected magnetic entropy, $S = \ln(2J + 1) = 95$ J/mole-K, for $J = 9/2$. S_{mag} has its largest drop over the temperature range corresponding to the Schottky-like peak in ΔC due to CEF splitting, while a further drop is observed near T_N. Magnetic heat capacity and entropy results are shown in Fig. 33.

Fig. 35 shows the magnetization of Nd_5NiPb_3 at two different fields. In the paramagnetic region, susceptibility can be fitted to a Curie-Weiss law with an effective magnetic moment $\mu_{eff} = 3.74$ μ_B per Nd, and a paramagnetic Curie temperature,

$\theta_p = +14.9$ K. The transition at 42 K, which is also seen in specific heat, is apparently antiferromagnetic due to its cusp-like shape and the decrease of the peak position with increasing field. However, the obvious hysteresis for field-cooled (FC) vs. zero-field-cooled (ZFC) data (inset, Fig. 35), and the general shape of the low-field magnetization curve corresponding to the lower transition, indicate ferrimagnetic behavior for this transition. Thus I assign this to a weak-ferromagnetic canting transition. The magnetizing curve measured at 2 K, showing a metamagnetic transition near 0.5 T, is consistent with such an analysis (see Fig. 34).

I also measured the resistivities, which have metallic temperature dependences for Nd_5NiPb_3 similar to the other materials measured here. I observed a sharp drop in the resistivity at 42 K corresponding to the reduction of spin-disorder scattering at the magnetic transitions. These data are not shown here.

d. Gd_5NiPb_3

In Gd_5NiPb_3 the heat capacity has a broad peak at 68 K corresponding to a long-range order ferro- or ferrimagnetic transition at that temperature, which is also consistent with a positive Curie-Weiss temperature (which will be discussed in next section). The low temperature specific heat data could be fit to $C = \gamma T + \beta T^3$, with a large γ of 626 mJ/mol-K^2 as shown in Fig. 36.

I isolated the magnetic contribution to the heat capacity (ΔC) by subtracting an interpolated La_5NiPb_3 curve from that of Gd_5NiPb_3. The resulting ΔC is shown in the inset of Fig. 37. The high temperature ΔC is reduced towards zero more quickly than in Nd and Ce samples, presumably due to the absence of crystalline electric fields, as expected because the Gd^{3+} total angular momentum L is zero. From (ΔC) we also obtained the magnetic entropy using the relation $S = \int (\Delta C/T)dT$. S reaches a plateau at high temperatures, which is approximately 40% of the expected value for

Fig. 35. Magnetization vs. temperature at different fields for Nd_5NiPb_3. The inset shows ZFC and FC magnetization.

Fig. 36. Heat capacity versus temperature for Gd_5NiPb_3 showing a peak at 68 K . In the inset, C/T data are plotted as a function of T^2, along with a linear fit.
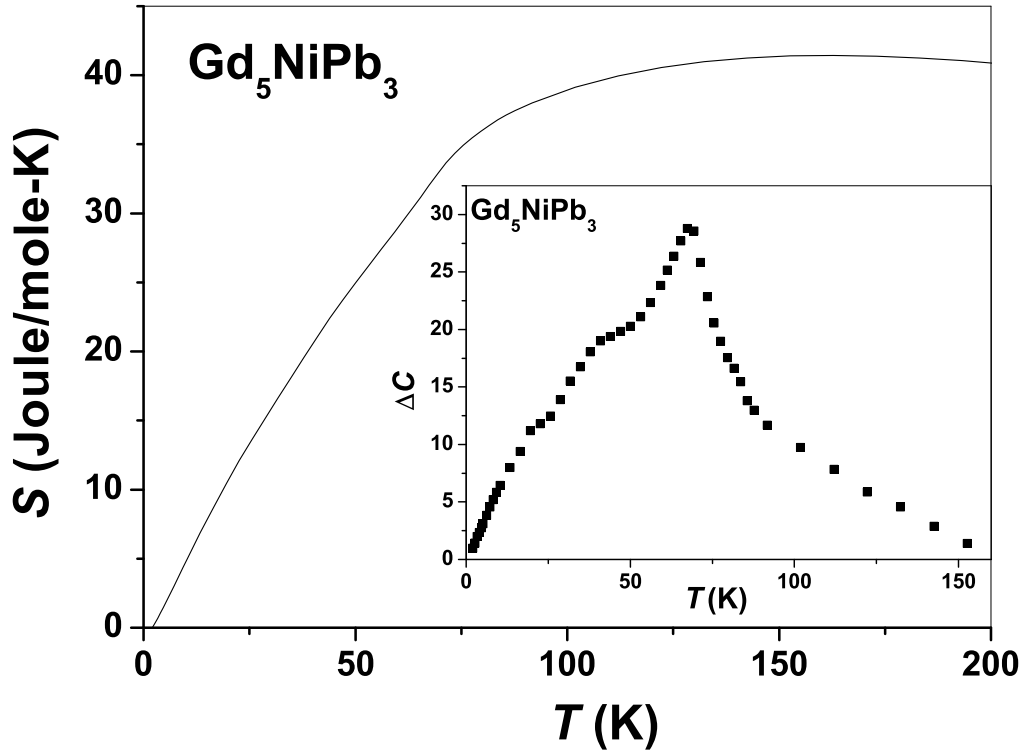
Fig. 37. Magnetic entropy as a function of temperature from difference as described in
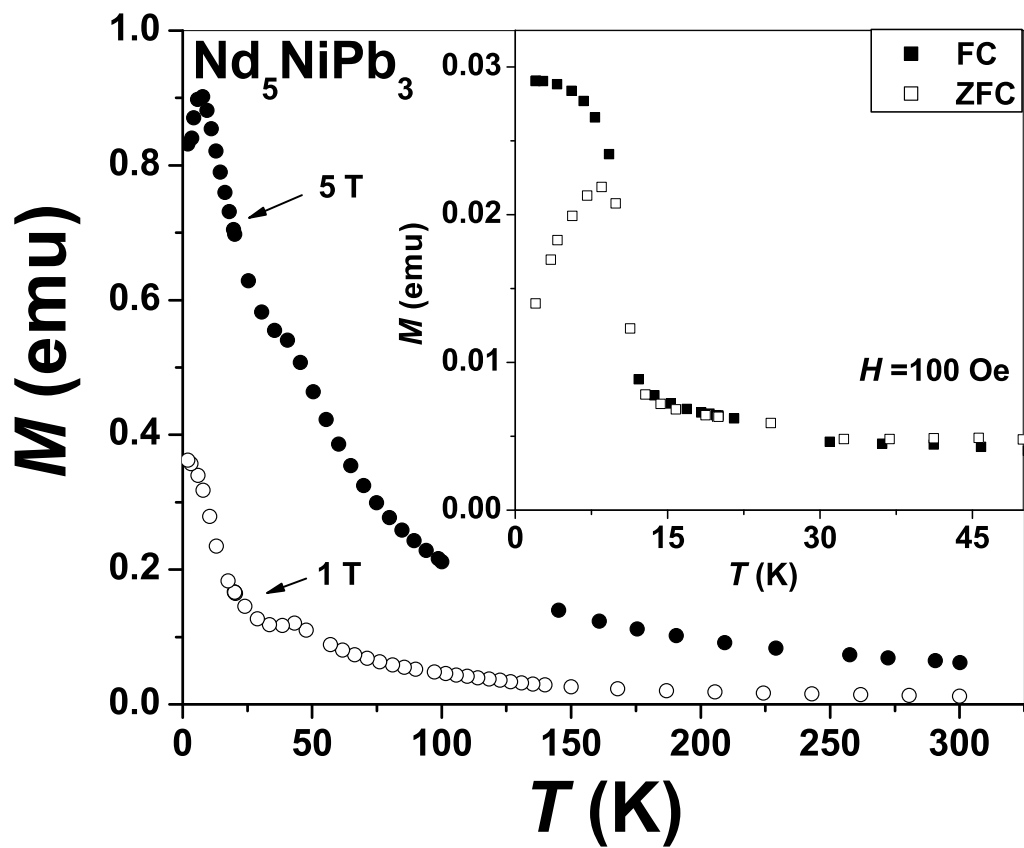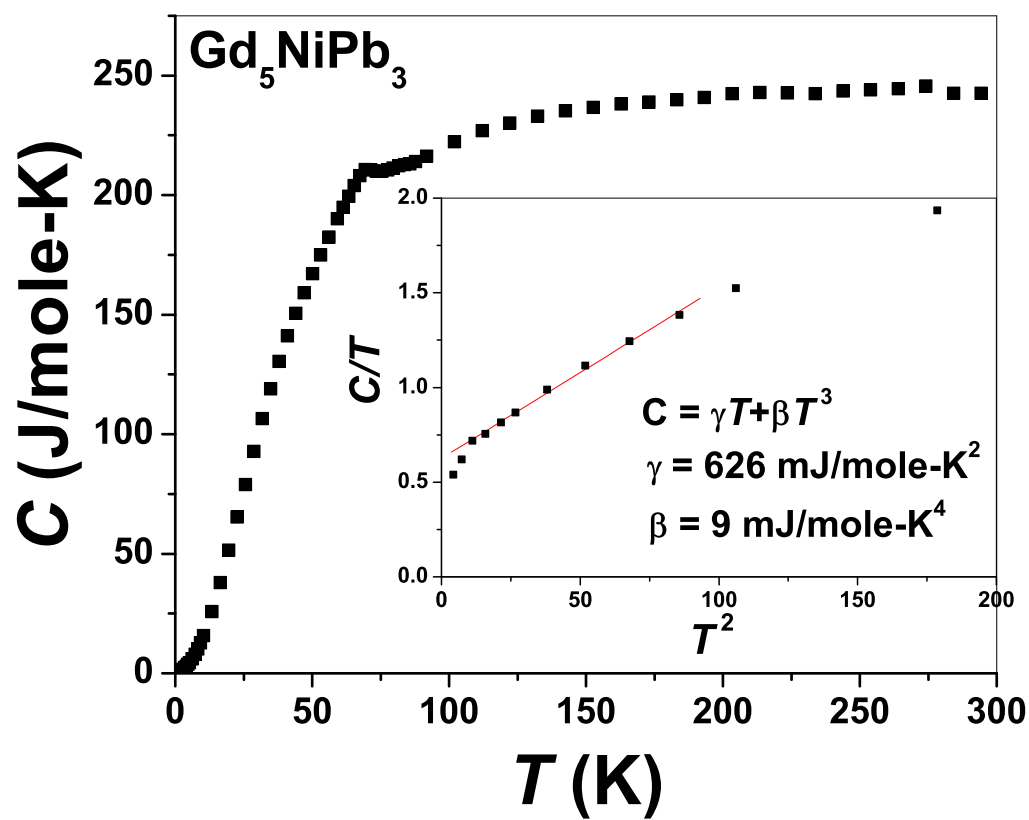text. In inset, plot of magnetic heat capacity versus temperature for Gd_5NiPb_3
showing a peak at 68 K.

J = 7/2 (Gd^{3+}). Fig. 37 shows the magnetic entropy as a function of temperature.

The Gd_5NiPb_3 ZFC and FC magnetization are shown in Fig. 38. A very sharp
irreversibility at 68 K is observed. At high T, the magnetization data follow a Curie-
Weiss law yielding an effective moment $8.9\mu_B$ as compared to the expected value of
$7.9\mu_B$. For this material, the 10% difference between experimental and theoretical
p_{eff} is due to the reasons not understood. The fitting results are shown in Fig. 39.
The value of the paramagnetic Curie temperature (θ_p) is +54 K as shown in Fig. 39.
The magnetization increases sharply near the transition at 68 K. The inset of Fig. 38
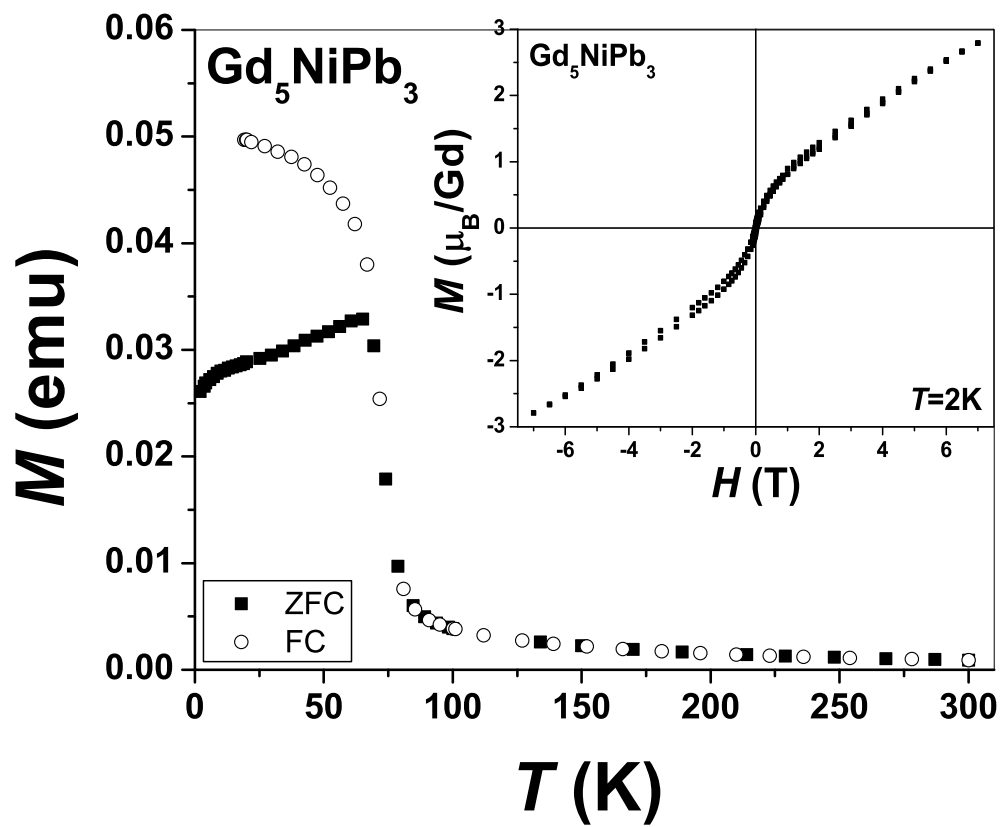
Fig. 38. ZFC and FC magnetization versus temperature for Gd_5NiPb_3 at field=100 Oe. The inset figure shows M vs. H loop.
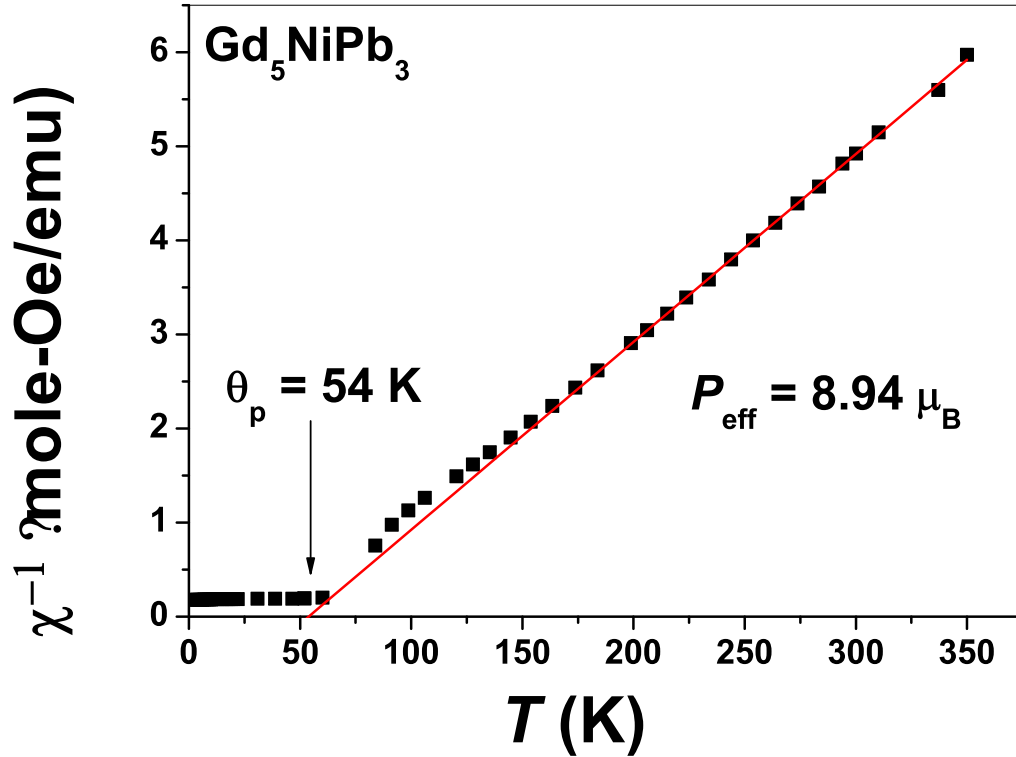
Fig. 39. χ^{-1} vs. T for Gd_5NiPb_3. Solid line is a Curie-Weiss fit, yielding the moment and Curie constant indicated.

shows a $M-H$ loop at 2 K, showing no saturation in a field of 7 T and with a small hysteresis. From these observations I conclude that this material is ferrimagnetic. This is also consistent with the heat capacity results.

Fig. 40 shows C vs. T of all three R_5NiPb_3 ($R=$ La, Ce,Nd and Gd) materials, showing peaks at the transition temperatures. The inset is zoomed for low temperature resolution. Fig. 41 compares magnetic S vs. T for the three magnetic materials, showing the saturation at high temperatures.

e. R_5NiPb$_3$ General Analysis

As shown above, these materials exhibit a variety of magnetic behavior. The transition temperatures are generally large, attributable presumably to the direct $R - R$ bonding in the structure. In these materials, lack of bulk magnetization saturation, high γ and ZFC, FC irreversibility have been observed. The specific heat for these materials leads to magnetic entropy changes that are more or less consistently one-half the expected value. This difference is definetely not due to mass corrections.

In some lattices, it is not possible to find a single ordered state which satisfies an AF interaction for all spins at all sites. Such a situation is referred to as frustrated spin system, and the result may be lack of magnetic order even though there is a sizable interaction between localized moments. Classic examples are the pyrochlore 3D and Kagome 2D lattices [41]. The latter contains linked triangles, while the former has linked terahedra. Considering simply the triangle, it is not possible to align all three spins so as to satisfy an AF interaction once two spins become ordered anti-parallel. The third is frustrated with no way to lower its energy. A similar situation can happen in the pyrochlore lattice where spins are on corner-sharing tetrahedra. A number of physical examples of such systems have been found which show irreversibility in ZFC and FC magnetization measurements, metastability and spin fluctuation behavior. Similar behavior has been observed in frustrated pyrochlore materials [42, 41].In some materials this frustration can also lead to spin fluctuations, where large γ and its suppression with magnetic field is observed [41]

Based on the above observations I have a model based on geometrical frustration that may account the results for the R_5NiPb$_3$ material. It may be that the site, which forms triangular antipyramid chains (shown in Fig. 4), does not order even at low temperatures due to frustration. This would explain both the reduced values of
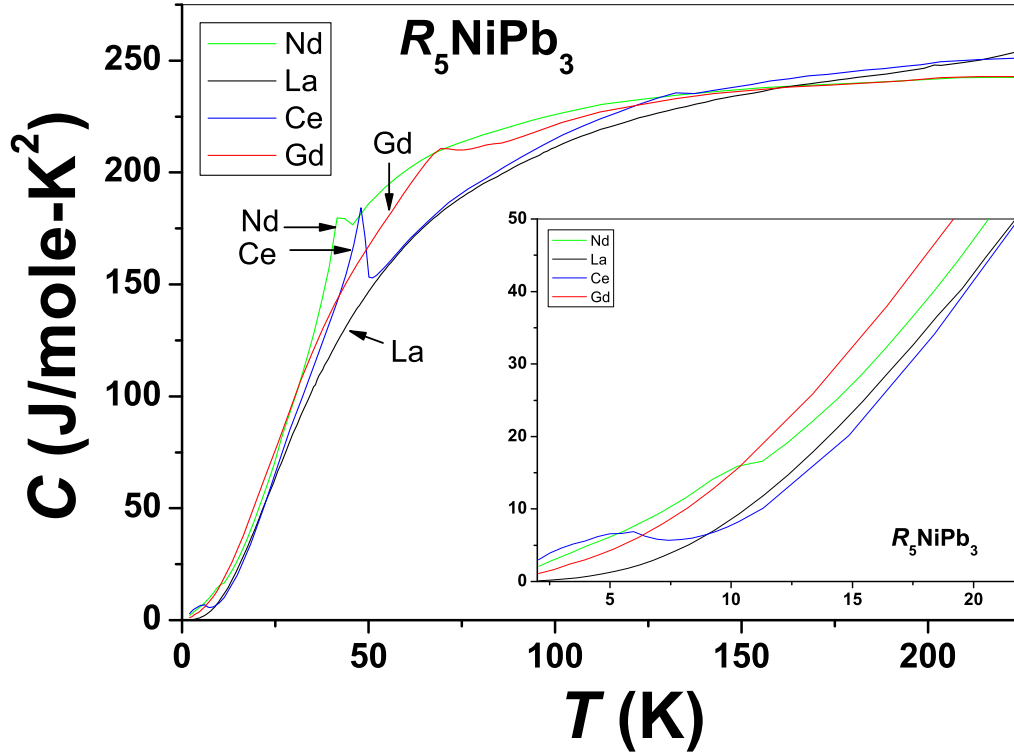
Fig. 40. Specific heat vs. T of R_5NiPb$_3$ ($R=$ La, Ce, Nd and Gd), showing peaks at the transition temperatures. Inset is zoomed for low temperature resolution.

entropy and the large γ values observed in these systems.

3. R_5NiPb$_3$ Conclusions

In summary I report susceptibility, heat capacity and electrical resistivity measurements on recently discovered R_5NiPb$_3$ ($R=$ La, Ce, Nd, Gd). I observed a variety of phase transitions in these materials. For example for Ce$_5$NiPb$_3$ a step like phase transition has been observed at 48 K. This transition indicates an apparent ferromagnetic transition, which is also confirmed by field dependent heat capacity and a positive Curie-Weiss temperature. Nd$_5$NiPb$_3$ exhibits two magnetic transitions, an

Fig. 41. Magnetic entropy, S, vs. T for R_5NiPb_3 ($R=$ Ce, Nd and Gd), showing saturation at high temperatures.

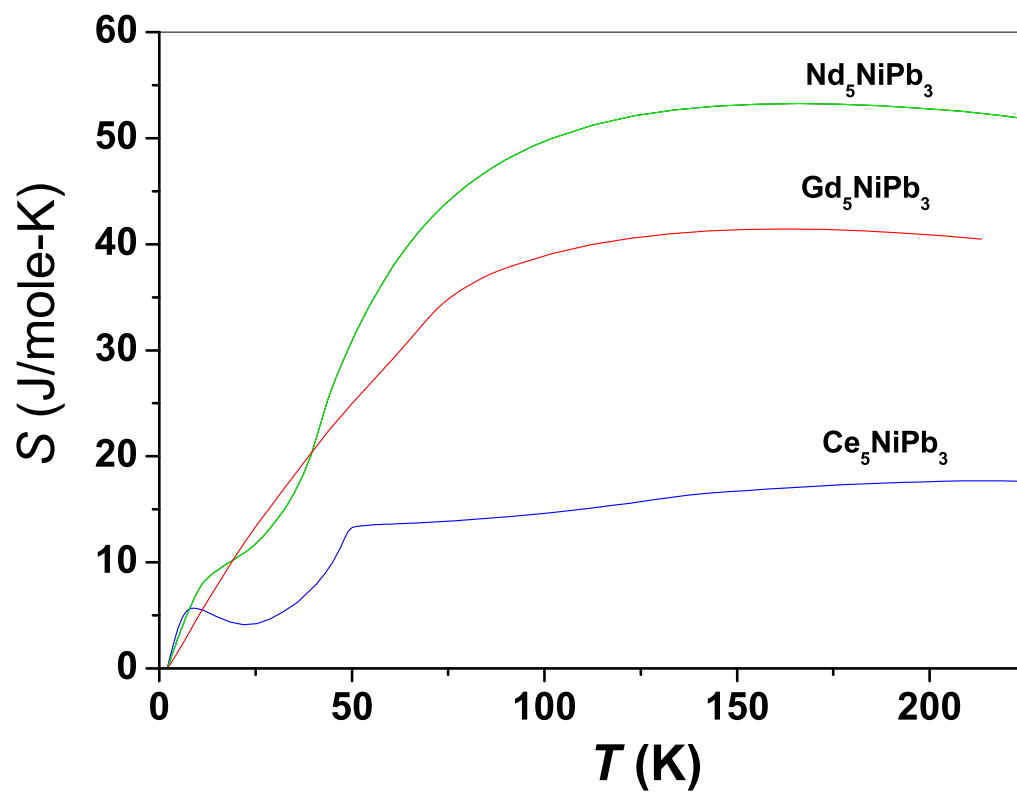antiferromagnetic transition at 42 K and an apparently weak ferromagnetic canting transition at 8 K. Magnetic heat capacity also shows a Schottky peak interrupted by magnetic transitions. Gd_5NiPb_3 shows a kink in both the magnetization and specific heat at 68 K indicating a ferrimagnetic transition at that temperature, which is confirmed by a positive Curie-Weiss temperature. For this material, ZFC and FC measurements show irreversibility at the transition temperature. The magnetic entropy change for all of the materials did not reach the theoretical value, saturating at approximately 50% of theoretical. I have also observed unusually high γ values in the specific heat even for the Nd compound. Such behavior is consistent with spin fluctuation behavior. I tentatively attributed these results to partial ordering at the phase transitions, with the three fold sites unaligned due to geometric frustration. These interesting results warrant further study, for example via neutron diffraction scattering, to explore the spatial nature of the magnetic phases.

CHAPTER VI

CONCLUSIONS

Nd_2Ni_2Pb heat capacity measurements indicate a sharp step-like antiferromagnetic phase transition at 19 K involving crystal-field-split levels. Magnetization measurements confirm this assignment, and reveal a spin-alignment meta-magnetic transition at 3 T. Observation of a single antiferromagnetic phase differs from the observed behavior of the heavier-rare-earth R_2Ni_2Pb materials.

NdNiPb susceptibility, heat capacity and electrical resistivity measurements show a clear magnetic phase transition found near 3.5 K however no superconductivity. With a combination of specific heat and magnetization, I also obtained a consistent estimation of the CEF splitting energy for NdNiPb, and showed that the ground state is composed of a doublet. Resistivity measurements showed metallic behavior.

NdCuGe magnetization is dominated by Nd^{3+} ionic moments at high temperatures, while at low temperatures CEF splitting of the rare-earth levels comes into play. With a combination of heat capacity, magnetization, and resistivity I obtained a consistent estimation of the CEF splitting energies, and show that the ground state is composed of a $J_z = 5/2$ doublet. Saturation measurements show that the previously-observed low-temperature magnetic state is formed from this doublet. The resistivity fit results are in good agreement with heat capacity and magnetization.

I also studied the R_5NiPb_3 (R = La, Ce, Nd, Gd) system and observed a variety of phase transitions in these materials. For example for Ce_5NiPb_3 a λ type phase transition has been observed at 48 K and a small feature at low T. At T=48 K transition indicates an apparent ferromagnetic transition, which is also confirmed by field dependent heat capacity and a positive Curie-Weiss temperature. Nd_5NiPb_3 exhibits two magnetic transitions, an antiferromagnetic transition at 42 K and an

apparently weak ferromagnetic canting transition at 8 K. Magnetic heat capacity also shown a Schottky peak interrupted by magnetic transitions. Gd_5NiPb_3 shows a kink in both the magnetization and specific heat at 68 K indicates a ferri-magnetic transition at that temperature, which is also confirmed by a positive Curie-Weiss temperature. For this material, ZFC and FC measurements show irreversibility at transition temperature. The magnetic entropy change for all of the materials did not reach the theoretical value, saturating at approximately 50% of theoretical. I have also observed unusually high γ values in the specific heat even for the Nd compound. Such behavior is consistent with spin fluctuation behavior. I tentatively attribute these results on R_5NiPb_3 to partial ordering at the phase transitions, with the three fold sites unaligned due to geometric frustration. These interesting results warrant further study, for example via neutron diffraction scattering, to explore the spatial nature of the magnetic phases.

REFERENCES

[1] D. Huo, T. Kuwai, Q. Lu, and Y. Isikawa, Phys. Rev. B **64**, 224405 (2001).

[2] C. Tien, C. H. Feng, C. S. Wur, and J. J. Lu, Phys. Rev. B **61**, 12151 (2001).

[3] A. D. Chinchure, E. Munoz-Sandoval, and J. A. Mydosh, Phys. Rev. B **64**, 020404 (2001).

[4] A. Szytula and J. Leciejewicz, *Handbook of Crystal Structures and Magnetic Properties of Rare Earth Intermetallics*, (CRC Press, New York, 1994).

[5] F. B. Anders and T. Pruschke, Phys. Rev. Lett. **96**, 086404 (2006).

[6] C. Kittel, *Introduction to Solid State Physics*, (John Wiley & Sons, Inc., New York, 1986).

[7] L. D. Gulay, Y. Kalychakb, M. Wolcyrz, and K. Lukaszewicz, J. Alloys Compd. **313**, 42 (2000).

[8] L. D. Gulay, Y. Kalychakb, and M. Wolcyrz, J. Alloys Compd. **311**, 228 (2000).

[9] L. D. Gulay and M. Wolcyrz, Pol. J. Chem. **75**, 1073 (2001).

[10] A. D. Chinchure, E. Munoz-Sandoval, and J. A. Mydosh, Phys. Rev. B **66**, 020409 (2002).

[11] E. Munoz-Sandoval, A. Diaz-Ortiz, A. D. Chinchure, and J. A. Mydosh, J. Alloys Compd. **369**, 260 (2004).

[12] V. Goruganti, Y. Li, J. H. Ross, Jr., K. D. D. Rathnayaka, and Y. Oner, J. Appl. Phys. **99**, 08P303 (2006).

[13] A. Szytula, D. Fus, B. Penc, and A. Jezierski, J. Alloys Compd. **317-318**, 340 (2001).

[14] C. P. Sebastian H. Eckert , C. Fehse, J. P. Wright , J. P. Attfield, D. Johrendt, S. Rayaprol , R. Hoffmann, and R. Pottgen, J. Solid State Chem. **179**, 2376 (2006).

[15] A. Iandelli, J. Alloys Compd. **198**, 141 (1993).

[16] S. Rayaprol, C. P. Sebastian, and R. Pottgen, J. Sol. State Chem. **179**, 2041 (2006).

[17] Y. Oner, O. Kamer, J. H. Ross, Jr., C. S. Lue, and Y. K. Kuo, Solid State Commun. **136**, 235 (2005).

[18] F. Yang J. P. Kuang, J. Li, E. Bruck, H. Nakotte, F. R. de Boer, X. Wu, Z. Li and Y. Wang, J. Appl. Phys **8**, 4705 (1991).

[19] V. Goruganti, K. D. D. Rathnayaka, J. H. Ross, Jr., Y. Oner, C. S. Lue, and Y. K. Kuo, J. Appl. Phys. **103**, 073919 (2008).

[20] S. Baran A. Szytula, J. Leciejewicz, N. Stusser, A. Zygmunt, Z. Tomkowicz, and M. Guillot, J. Alloys Compd. **243**, 112 (1996).

[21] L. D. Gulay, J. Alloys Compd. **392**, 165 (2005).

[22] V. Goruganti, K. D. D. Rathnayaka, Y. Oner, and J. H. Ross, Jr., J. Appl. Phys. **99**, 07B709 (2008).

[23] A. Tari, *The Specific Heat of Matter at Low Temperatures*, (Imperial College Press, London, 2003).

[24] E. S. R. Gopal, *Specific Heats at Low Temperatures*, (Plenum, New York, 1996).

[25] M. Endo, I. Umehara, Y. Adachi, Y. Isikawa, and K. Sato, Mater. Trans., JIM **41**, 452 (2000).

[26] J. E. Gordon R. A. Fisher, Y. X. Jia, N. E. Phillips, S. F. Reklis, D. A. Wright, and A. Zettl, Phys. Rev. B **59**, 127 (1999).

[27] O. V. Lounasmaa and L. J. Sundström, Phys. Rev. **158**, 591 (1967).

[28] A. H. Morrish, *The Physical Principles of Magnetism*, (John Wiley & Sons, Inc., New York, 1965).

[29] S. Chikazumi and C. D. Graham, *Physics of Ferromagnetism*, (Oxford University Press, New York, 1997).

[30] J. Chi, F. G. Vagizov, V. Goruganti, and J. H. Ross, Jr., Phys. Rev. B **71**, 024431 (2005).

[31] P. Blaha, K. Schwarz, G. Madsen, D. Kvasnicka, and J. Luitz, Computer Code WIEN2K, Technical Report, Vienna University of Technology, Austria, 2001.

[32] Y. Öner, V. Goruganti, O. Kamer, M. Guillot, and J. Joseph H. Ross, J. Appl. Phys. **103**, 07B915 (2008).

[33] A. C. Larson and R. B. von Dreele, General structure analysis system (gsas), Technical Report LAUR 86-748, Los Alamos National Laboratory, 2000.

[34] B. H. Toby, J. Appl. Cryst. **34**, 210 (2001).

[35] Y. Oner, private communication, 2007.

[36] L. D. Gulay and K. Hiebl, J. Alloys Compd. **339**, 46 (2002).

[37] D. J. Newman and B. Ng, editors, *Crystal Field Handbook*, (Cambridge University Press, Cambridge, UK, 2000).

[38] M. Bouvier, P. Lethuillier, and D. Schmitt, Phys. Rev. B **43**, 13137 (1991).

[39] D. Vollhardt, Phys. Rev. Lett. **78**, 1307 (1997).

[40] M. E. Huntelaar, A. S. Booji, E. H. P. Cordefunke, and V. R. R. Laan, J. Chem. Thermodynamics **32**, 465 (2000).

[41] S. T. Bramwell and M. J. P. Gingras, Science **294**, 1495 (2001).

[42] A. P. Ramirez, A. Hayashi, R. J. Cava, R. Siddharthan, and B. S. Shastry, Nature **399**, 333 (1999).

VITA

Venkateshwarlu Goruganti,

vgoruganti at gmail.com

Physics, Texas A&M University,

College Station, TX 77843-4242

Education:

Ph.D., Physics, Texas A&M University	Dec 2008
M. S., Material Science & Engineering, Texas A&M University	Aug 2005
M. Sc., Physics, University of Hyderabad, India	May 2001
B. Ed., Physical Science, Osmania University, India	May 1999
B. Sc., Physics, Osmania University, India	May 1998

Journal Publications while doing PhD:

1. *V. Goruganti*, K. D. D. Rathnayaka, Y. Oner, C. S. Lue, Y. K. Kuo and Joseph H. Ross, Jr., *J. Appl. Phys.* 103, 073919 (2008)

2. *V. Goruganti*, K. D. D. Rathnayaka, Y. Oner, and Joseph H. Ross, Jr., *J. Appl. Phys.* 103, 07B709 (2008)

3. Y. Oner, *V. Goruganti*, O. Kamer, M. Guillot, and Joseph H. Ross, Jr., *J. Appl. Phys.* 103, 07B915 (2008)

4. Ji Chi, Yang Li, Weiping Gou, *V. Goruganti*, K. D. D. Rathnayaka, Joseph H. Ross, Jr. *Physica B* 403, 1426 (2008)

5. *V. Goruganti*, Yang Li, Joseph H. Ross, Jr., K. D. D. Rathnayaka, and Y. Oner, *J. Appl. Phys.* 99, 08P303 (2006)

6. Ji Chi, Yang Li, F. G. Vagizov, *V. Goruganti*, and Joseph H. Ross, Jr., *Phys. Rev. B* 71, 024431 (2005)

7. Yang Li, Weiping Gou, Ji Chi, *V. Goruganti*, and Joseph H. Ross, Jr., *AIP Conf. Proc.* 772, 331 (2005)

8. *V. Goruganti*, K. D. D. Rathnayaka, and Joseph H. Ross, Jr., (sub. to *JAP*)